

Measurement of the absolute branching fractions for purely leptonic D_s^+ decays

M. Ablikim(麦迪娜)¹, M. N. Achasov^{10,c}, P. Adlarson⁶⁷, S. Ahmed¹⁵, M. Albrecht⁴, R. Aliberti²⁸, A. Amoroso^{66A,66C}, M. R. An(安美儒)³², Q. An(安琪)^{49,63}, X. H. Bai(白旭红)⁵⁷, Y. Bai(白羽)⁴⁸, O. Bakina²⁹, R. Baldini Ferroli^{23A}, I. Balossino^{24A,1}, Y. Ban(班勇)^{38,k}, K. Begzsuren²⁶, N. Berger²⁸, M. Bertani^{23A}, D. Bettoni^{24A}, F. Bianchi^{66A,66C}, J. Bloms⁶⁰, A. Bortone^{66A,66C}, I. Boyko²⁹, R. A. Briere⁵, H. Cai(蔡浩)⁶⁸, X. Cai(蔡啸)^{1,49}, A. Calcaterra^{23A}, G. F. Cao(曹国富)^{1,54}, N. Cao(曹宁)^{1,54}, S. A. Cetin^{53B}, J. F. Chang(常劭帆)^{1,49}, W. L. Chang(常万玲)^{1,54}, G. Chelkov^{29,b}, D. Y. Chen(陈端友)⁶, G. Chen(陈刚)¹, H. S. Chen(陈和生)^{1,54}, M. L. Chen(陈玛丽)^{1,49}, S. J. Chen(陈申见)³⁵, X. R. Chen(陈旭荣)²⁵, Y. B. Chen(陈元柏)^{1,49}, Z. J. Chen(陈卓俊)^{20,l}, W. S. Cheng(成伟帅)^{66C}, G. Cibinetto^{24A}, F. Cossio^{66C}, X. F. Cui(崔小非)³⁶, H. L. Dai(代洪亮)^{1,49}, X. C. Dai(戴鑫琛)^{1,54}, A. Dbeyssi¹⁵, R. E. de Boer⁴, D. Dedovich²⁹, Z. Y. Deng(邓子艳)¹, A. Denig²⁸, I. Denysenko²⁹, M. Destefanis^{66A,66C}, F. De Mori^{66A,66C}, Y. Ding(丁勇)³³, C. Dong(董超)³⁶, J. Dong(董静)^{1,49}, L. Y. Dong(董燎原)^{1,54}, M. Y. Dong(董明义)¹, X. Dong(董翔)⁶⁸, S. X. Du(杜书先)⁷¹, Y. L. Fan(范玉兰)⁶⁸, J. Fang(方建)^{1,49}, S. S. Fang(房双世)^{1,54}, Y. Fang(方易)¹, R. Farinelli^{24A}, L. Fava^{66B,66C}, F. Feldbauer⁴, G. Felici^{23A}, C. Q. Feng(封常青)^{49,63}, J. H. Feng⁵⁰, M. Fritsch⁴, C. D. Fu(傅成栋)¹, Y. Gao(高雅)⁶⁴, Y. Gao(高扬)^{49,63}, Y. Gao(高原宁)^{38,k}, Y. G. Gao(高勇贵)⁶, I. Garzia^{24A,24B}, P. T. Ge(葛潘婷)⁶⁸, C. Geng(耿聪)⁵⁰, E. M. Gersabeck⁵⁸, A. Gilman⁶¹, K. Goetzen¹¹, L. Gong³³, W. X. Gong(龚文煊)^{1,49}, P. W. Gradl²⁸, M. Greco^{66A,66C}, L. M. Gu(谷立民)³⁵, M. H. Gu(顾皓)^{1,49}, S. Gu(顾珊)², Y. T. Gu(顾运斤)¹³, C. Y. Guan(关春懿)^{1,54}, A. Q. Guo(郭爱强)²², L. B. Guo(郭立波)³⁴, R. P. Guo(郭如盼)⁴⁰, Y. P. Guo^{9,h}, A. Guskov²⁹, T. T. Han(韩婷婷)⁴¹, W. Y. Han(韩文颖)³², X. Q. Hao(郝喜庆)¹⁶, F. A. Harris⁵⁶, N. H. Üsküden^{22,28}, K. L. He(何康林)^{1,54}, F. H. Heinsius⁴, C. H. Heinz²⁸, T. Held⁴, Y. K. Heng(衡月昆)¹, C. Herold⁵¹, M. Himmelreich^{11,f}, T. Holtmann⁴, Y. R. Hou(侯颖锐)⁵⁴, Z. L. Hou(侯治龙)¹, H. M. Hu(胡海明)^{1,54}, J. F. Hu⁴⁷, T. Hu(胡涛)¹, Y. Hu(胡誉)¹, G. S. Huang(黄光顺)^{49,63}, L. Q. Huang(黄麟毅)⁶⁴, X. T. Huang(黄性涛)⁴¹, Y. P. Huang(黄燕萍)¹, Z. Huang(黄震)^{38,k}, T. Hussain⁶⁵, W. Ikegami Andersson⁶⁷, W. Imoehl²², M. Irshad^{49,63}, S. Jaeger⁴, S. Janchiv^{26,j}, Q. Ji(纪全)¹, Q. P. Ji(姬清平)¹⁶, X. B. Ji(季晓斌)^{1,54}, X. L. Ji(季筱璐)^{1,49}, Y. Y. Ji⁴¹, H. B. Jiang(姜侯兵)⁴¹, X. S. Jiang(江晓山)¹, J. B. Jiao(焦健斌)⁴¹, Z. Jiao(焦铮)¹⁸, S. Jin(金山)³⁵, Y. Jin(金毅)⁵⁷, T. Johansson⁶⁷, N. Kalantar-Navestanaki⁵⁵, X. S. Kang(康晓)³³, R. Kappert⁵⁵, M. Kavatsyuk⁵⁵, B. C. Ke(柯百谦)^{1,43}, I. K. Keshk⁴, A. Khokkaz⁶⁰, P. Kiese²⁸, R. Kiuchi¹, R. Kliemt¹¹, L. Koch³⁰, O. B. Kolcu^{53B,e}, B. Kopf⁴, M. Kuemmel⁴, M. Kuessner⁴, A. Kupsc⁶⁷, M. G. Kurth^{1,54}, W. Kühn³⁰, J. J. Lane⁵⁸, J. S. Lange³⁰, P. Larin¹⁵, A. Lavania²¹, L. Lavezzi^{66A,66C,1}, Z. H. Lei(雷祚弘)^{49,63}, H. Leithoff²⁸, M. Lellmann²⁸, T. Lenz²⁸, C. Li(李翠)³⁹, C. H. Li(李春花)³², Cheng Li(李澄)^{49,63}, D. M. Li(李德民)⁷¹, F. Li(李飞)^{1,49}, G. Li(李刚)¹, H. Li(李慧)⁴³, H. Li(李贺)^{49,63}, H. B. Li(李海波)^{1,54}, H. J. Li(李惠静)^{9,h}, H. J. Li(李惠静)¹⁶, J. L. Li(李井文)⁴¹, J. Q. Li⁴, J. S. Li(李静舒)⁵⁰, Ke Li(李科)¹, L. K. Li(李龙科)¹, Lei Li(李蕾)³, P. R. Li(李培荣)³¹, S. Y. Li(栗帅迎)⁵², W. D. Li(李卫东)^{1,54}, W. G. Li(李卫国)¹, X. H. Li(李旭红)^{49,63}, X. L. Li(李晚玲)⁴¹, Xiaoyu Li(李晚宇)^{1,54}, Z. Y. Li(李紫源)⁵⁰, H. Liang(梁昊)^{49,63}, H. Liang(梁浩)^{1,54}, H. Liang(梁浩)²⁷, Y. F. Liang(梁勇飞)⁴⁵, Y. T. Liang(梁羽铁)²⁵, G. R. Liao(廖广睿)¹², L. Z. Liao(廖龙洲)^{1,54}, J. Libby²¹, C. X. Lin(林创新)⁵⁰, B. J. Liu(刘北江)¹, C. X. Liu(刘春秀)¹, D. Liu(刘栋)^{49,63}, F. H. Liu(刘福虎)⁴⁴, Fang Liu(刘芳)¹, Feng Liu(刘峰)⁶, H. B. Liu(刘宏邦)¹³, H. M. Liu(刘怀民)^{1,54}, Huanhuan Liu(刘欢欢)¹, Huihui Liu(刘汇慧)¹⁷, J. B. Liu(刘建北)^{49,63}, J. L. Liu(刘佳俊)⁶⁴, J. Y. Liu(刘晶译)^{1,54}, K. Liu(刘凯)¹, K. Y. Liu(刘魁勇)³³, Ke Liu(刘珂)⁶, L. Liu(刘亮)^{49,63}, M. H. Liu^{9,h}, P. L. Liu(刘佩莲)¹, Q. Liu(刘倩)⁵⁴, Q. Liu(刘淇)⁶⁸, S. B. Liu(刘树彬)^{49,63}, Shuai Liu(刘帅)⁴⁶, T. Liu(刘桐)^{1,54}, W. M. Liu(刘卫民)^{49,63}, X. Liu(刘翔)³¹, Y. Liu³¹, Y. B. Liu(刘玉斌)³⁶, Z. A. Liu(刘振安)¹, Z. Q. Liu(刘智青)⁴¹, X. C. Lou(娄辛丑)¹, F. X. Lu(卢飞翔)¹⁶, F. X. Lu⁵⁰, H. J. Lu(吕海江)¹⁸, J. D. Lu(陆嘉达)^{1,54}, J. G. Lu(吕军光)^{1,49}, X. L. Lu(陆小玲)¹, Y. Lu(卢宇)¹, Y. P. Lu(卢云鹏)^{1,49}, C. L. Luo(罗成林)³⁴, M. X. Luo(罗民兴)⁷⁰, P. W. Luo(罗朋威)⁵⁰, T. Luo(罗涛)^{9,h}, X. L. Luo(罗小兰)^{1,49}, S. Lusso^{66C}, X. R. Lyu(吕晓睿)⁵⁴, F. C. Ma(马凤才)³³, H. L. Ma(马海龙)¹, L. L. Ma(马连良)⁴¹, M. M. Ma(马明明)^{1,54}, Q. M. Ma(马秋梅)¹, R. Q. Ma(马润秋)^{1,54}, R. T. Ma(马瑞廷)⁵⁴, X. X. Ma(马新鑫)^{1,54}, X. Y. Ma(马晓妍)^{1,49}, F. E. Maas¹⁵, M. Maggiora^{66A,66C}, S. Maldaner⁴, S. Malde⁶¹, Q. A. Malik⁶⁵, A. Mangoni^{23B}, Y. J. Mao(冒亚军)^{38,k}, Z. P. Mao(毛泽普)¹, S. Marcello^{66A,66C}, Z. X. Meng(孟召霞)⁵⁷, J. G. Messchendorp⁵⁵, G. Mezzadri^{24A,1}, T. J. Min(闵天觉)³⁵, R. E. Mitchell²², X. H. Mo(莫晓虎)¹, Y. J. Mo(莫玉俊)⁶, N. Yu. Muchnoi^{10,c}, H. Muramatsu(村松创)⁵⁹, S. Nakhoul^{11,f}, Y. Nefedov²⁹, F. Nerling^{11,f}, I. B. Nikolaev^{10,c}, Z. Ning(宁哲)^{1,49}, S. Nisar^{8,i}, S. L. Olsen(马鹏)⁵⁴, Q. Ouyang(欧阳群)¹, S. Pacetti^{23B,23C}, X. Pan^{9,h}, Y. Pan⁵⁸, A. Pathak¹, P. Patteri^{23A}, M. Pelizaeus⁴, H. P. Peng(彭海平)^{49,63}, K. Peters^{11,f}, J. Pettersson⁶⁷, J. L. Ping(平加伦)³⁴, R. G. Ping(平荣刚)^{1,54}, R. Poling⁵⁹, V. Prasad^{49,63}, H. Qi(齐航)^{49,63}, H. R. Qi(漆红琴)⁵², K. H. Qi(祁康辉)²⁵, M. Qi(祁鸣)³⁵, T. Y. Qi(齐天钰)², T. Y. Qi⁹, S. Qian(钱森)^{1,49}, W. B. Qian(钱文斌)⁵⁴, Z. Qian(钱圳)⁵⁰, C. F. Qiao(乔从丰)⁵⁴, L. Q. Qin(秦丽清)¹², X. P. Qin(覃潇平)⁹, X. S. Qin⁴¹, Z. H. Qin(秦中华)^{1,49}, J. F. Qiu(邱进发)¹, S. Q. Qu(屈三强)³⁶, K. H. Rashid⁶⁵, K. Ravindran²¹, C. F. Redmer²⁸, A. Rivetti^{66C}, V. Rodin⁵⁵, M. Rolo^{66C}, G. Rong(荣刚)^{1,54}, Ch. Rosner¹⁵, M. Rump⁶⁰, H. S. Sang(桑昊榆)⁶³, A. Sarantsev^{29,d}, Y. Schelhaas²⁸, C. Schnier⁴, K. Schoenning⁶⁷, M. Scodreggio^{24A,24B}, D. C. Shan(单多琛)⁴⁶, W. Shan(单威)¹⁹, X. Y. Shan(单心钰)^{49,63}, J. F. Shangguan(上官剑锋)⁴⁶, M. Shao(邵明)^{49,63}, C. P. Shen⁹, P. X. Shen(沈培迅)³⁶, X. Y. Shen(沈肖雁)^{1,54}, H. C. Shi(石煌超)^{49,63}, R. S. Shi(师荣盛)^{1,54}, X. Shi(史欣)^{1,49}, X. D. Shi(师晓东)^{49,63}, J. J. Song(宋娇娇)⁴¹, W. M. Song(宋维民)^{1,27}, Y. X. Song(宋韵轩)^{38,k}, S. Sosio^{66A,66C}, S. Spataro^{66A,66C}, K. X. Su(苏可馨)⁶⁸, P. P. Su(苏彭彭)⁴⁶, F. F. Sui(隋风飞)⁴¹, G. X. Sun(孙功星)¹, H. K. Sun(孙浩凯)¹, J. F. Sun(孙俊峰)¹⁶, L. Sun(孙亮)⁶⁸, S. S. Sun(孙胜森)^{1,54}, T. Sun(孙童)^{1,54}, W. Y. Sun(孙文玉)³⁴, W. Y. Sun²⁷, X. Sun(孙翔)^{20,l}, Y. J. Sun(孙勇杰)^{49,63}, Y. K. Sun(孙艳坤)^{49,63}, Y. Z. Sun(孙永昭)¹, Z. T. Sun(孙振田)¹, Y. H. Tan(谭英华)⁶⁸, Y. X. Tan(谭雅星)^{49,63}, C. J. Tang(唐昌建)⁴⁵, G. Y. Tang(唐光毅)¹, J. Tang(唐健)⁵⁰, J. X. Teng(滕佳秀)^{49,63}, V. Thoren⁶⁷, Y. T. Tian(田野)²⁵, I. Uman^{53D}, B. Wang(王斌)¹, C. W. Wang(王成伟)³⁵, D. Y. Wang(王大勇)^{38,k}, H. J. Wang³¹, H. P. Wang(王宏鹏)^{1,54}, K. Wang(王科)^{1,49}, L. L. Wang(王亮亮)¹, M. Wang(王萌)⁴¹, M. Z. Wang^{38,k}, Meng Wang(王蒙)^{1,54}, W. Wang⁵⁰, W. H. Wang(王文欢)⁶⁸, W. P. Wang(王维平)^{49,63}, X. Wang^{38,k}, X. F. Wang(王雄飞)³¹, X. L. Wang^{9,h}, Y. Wang(王越)^{49,63}, Y. Wang(王莹)⁵⁰, Y. D. Wang³⁷, Y. F. Wang(王貽芳)¹, Y. Q. Wang(王雨晴)¹, Y. Y. Wang³¹, Z. Wang(王铮)^{1,49}, Z. Y. Wang(王至勇)¹, Ziyi Wang(王子一)⁵⁴, Zongyuan Wang(王宗

源)^{1,54}, D. H. Wei(魏代会)¹², P. Weidenkaff²⁸, F. Weidner⁶⁰, S. P. Wen(文硕频)¹, D. J. White⁵⁸, U. Wiedner⁴, G. Wilkinson⁶¹, M. Wolke⁶⁷, L. Wollenberg⁴, J. F. Wu(吴金飞)^{1,54}, L. H. Wu(伍灵慧)¹, L. J. Wu(吴连近)^{1,54}, X. Wu^{9,h}, Z. Wu(吴智)^{1,49}, L. Xia(夏磊)^{49,63}, H. Xiao^{9,h}, S. Y. Xiao(肖素玉)¹, Z. J. Xiao(肖振军)³⁴, X. H. Xie(谢昕海)^{38,k}, Y. G. Xie(谢宇广)^{1,49}, Y. H. Xie(谢跃红)⁶, T. Y. Xing(邢天宇)^{1,54}, G. F. Xu(许国发)¹, Q. J. Xu(徐庆君)¹⁴, W. Xu(许威)^{1,54}, X. P. Xu(徐新平)⁴⁶, Y. C. Xu(胥英超)⁵⁴, F. Yan^{9,h}, L. Yan^{9,h}, W. B. Yan(鄢文标)^{49,63}, W. C. Yan(闫文成)⁷¹, Xu Yan(闫旭)⁴⁶, H. J. Yang(杨海军)^{42,g}, H. X. Yang(杨洪勋)¹, L. Yang(杨玲)⁴³, S. L. Yang⁵⁴, Y. X. Yang(杨永翔)¹², Yifan Yang(杨翔凡)^{1,54}, Zhi Yang(杨智)²⁵, M. Ye(叶梅)^{1,49}, M. H. Ye(叶铭汉)⁷, J. H. Yin(殷俊昊)¹, Z. Y. You(尤郑昀)⁵⁰, B. X. Yu(俞伯祥)¹, C. X. Yu(喻纯旭)³⁶, G. Yu(余刚)^{1,54}, J. S. Yu(俞洁晟)^{20,l}, T. Yu(于涛)⁶⁴, C. Z. Yuan(苑长征)^{1,54}, L. Yuan(袁丽)², X. Q. Yuan^{38,k}, Y. Yuan(袁野)¹, Z. Y. Yuan(袁朝阳)⁵⁰, C. X. Yue³², A. Yuncu^{53B,a}, A. A. Zafar⁶⁵, Y. Zeng(曾云)^{20,l}, B. X. Zhang(张丙新)¹, Guangyi Zhang(张广义)¹⁶, H. Zhang⁶³, H. H. Zhang(张宏浩)⁵⁰, H. H. Zhang²⁷, H. Y. Zhang(章红宇)^{1,49}, J. J. Zhang(张进军)⁴³, J. L. Zhang(张杰磊)⁶⁹, J. Q. Zhang³⁴, J. W. Zhang(张家文)¹, J. Y. Zhang(张建勇)¹, J. Z. Zhang(张景芝)^{1,54}, Jianyu Zhang(张剑宇)^{1,54}, Jiawei Zhang(张嘉伟)^{1,54}, L. M. Zhang(张黎明)⁵², L. Q. Zhang(张丽青)⁵⁰, Lei Zhang(张雷)³⁵, S. Zhang(张澍)⁵⁰, S. F. Zhang(张思凡)³⁵, Shulei Zhang^{20,l}, X. D. Zhang³⁷, X. Y. Zhang(张学尧)⁴¹, Y. Zhang⁶¹, Y. H. Zhang(张银鸿)^{1,49}, Y. T. Zhang(张亚腾)^{49,63}, Yan Zhang(张言)^{49,63}, Yao Zhang(张瑶)¹, Yi Zhang^{9,h}, Z. H. Zhang(张正好)⁶, Z. Y. Zhang(张振宇)⁶⁸, G. Zhao(赵光)¹, J. Zhao(赵静)³², J. Y. Zhao(赵静宜)^{1,54}, J. Z. Zhao(赵京周)^{1,49}, Lei Zhao(赵雷)^{49,63}, Ling Zhao(赵玲)¹, M. G. Zhao(赵明刚)³⁶, Q. Zhao(赵强)¹, S. J. Zhao(赵书俊)⁷¹, Y. B. Zhao(赵豫斌)^{1,49}, Y. X. Zhao(赵宇翔)²⁵, Z. G. Zhao(赵治国)^{49,63}, A. Zhemchugov^{29,b}, B. Zheng(郑波)⁶⁴, J. P. Zheng(郑建平)^{1,49}, Y. Zheng^{38,k}, Y. H. Zheng(郑阳恒)⁵⁴, B. Zhong(钟彬)³⁴, C. Zhong(钟翠)⁶⁴, L. P. Zhou(周利鹏)^{1,54}, Q. Zhou(周巧)^{1,54}, X. Zhou(周详)⁶⁸, X. K. Zhou(周晓康)⁵⁴, X. R. Zhou(周小蓉)^{49,63}, X. Y. Zhou(周兴玉)³², A. N. Zhu(朱傲男)^{1,54}, J. Zhu(朱江)³⁶, K. Zhu(朱凯)¹, K. J. Zhu(朱科军)¹, S. H. Zhu(朱世海)⁶², T. J. Zhu⁶⁹, W. J. Zhu(朱文静)³⁶, W. J. Zhu^{9,h}, Y. C. Zhu(朱莹春)^{49,63}, Z. A. Zhu(朱自安)^{1,54}, B. S. Zou(邹冰松)¹, J. H. Zou(邹佳恒)¹

(BESIII Collaboration)

¹ Institute of High Energy Physics, Beijing 100049, People's Republic of China

² Beihang University, Beijing 100191, People's Republic of China

³ Beijing Institute of Petrochemical Technology, Beijing 102617, People's Republic of China

⁴ Bochum Ruhr-University, D-44780 Bochum, Germany

⁵ Carnegie Mellon University, Pittsburgh, Pennsylvania 15213, USA

⁶ Central China Normal University, Wuhan 430079, People's Republic of China

⁷ China Center of Advanced Science and Technology, Beijing 100190, People's Republic of China

⁸ COMSATS University Islamabad, Lahore Campus, Defence Road, Off Raiwind Road, 54000 Lahore, Pakistan

⁹ Fudan University, Shanghai 200443, People's Republic of China

¹⁰ G.I. Budker Institute of Nuclear Physics SB RAS (BINP), Novosibirsk 630090, Russia

¹¹ GSI Helmholtzcentre for Heavy Ion Research GmbH, D-64291 Darmstadt, Germany

¹² Guangxi Normal University, Guilin 541004, People's Republic of China

¹³ Guangxi University, Nanning 530004, People's Republic of China

¹⁴ Hangzhou Normal University, Hangzhou 310036, People's Republic of China

¹⁵ Helmholtz Institute Mainz, Johann-Joachim-Becher-Weg 45, D-55099 Mainz, Germany

¹⁶ Henan Normal University, Xinxiang 453007, People's Republic of China

¹⁷ Henan University of Science and Technology, Luoyang 471003, People's Republic of China

¹⁸ Huangshan College, Huangshan 245000, People's Republic of China

¹⁹ Hunan Normal University, Changsha 410081, People's Republic of China

²⁰ Hunan University, Changsha 410082, People's Republic of China

²¹ Indian Institute of Technology Madras, Chennai 600036, India

²² Indiana University, Bloomington, Indiana 47405, USA

²³ (A)INFN Laboratori Nazionali di Frascati, I-00044, Frascati, Italy; (B)INFN Sezione di Perugia, I-06100, Perugia, Italy; (C)University of Perugia, I-06100, Perugia, Italy

²⁴ (A)INFN Sezione di Ferrara, I-44122, Ferrara, Italy; (B)University of Ferrara, I-44122, Ferrara, Italy

²⁵ Institute of Modern Physics, Lanzhou 730000, People's Republic of China

²⁶ Institute of Physics and Technology, Peace Ave. 54B, Ulaanbaatar 13330, Mongolia

²⁷ Jilin University, Changchun 130012, People's Republic of China

²⁸ Johannes Gutenberg University of Mainz, Johann-Joachim-Becher-Weg 45, D-55099 Mainz, Germany

²⁹ Joint Institute for Nuclear Research, 141980 Dubna, Moscow region, Russia

³⁰ Justus-Liebig-Universität Giessen, II. Physikalisches Institut, Heinrich-Buff-Ring 16, D-35392 Giessen, Germany

³¹ Lanzhou University, Lanzhou 730000, People's Republic of China

³² Liaoning Normal University, Dalian 116029, People's Republic of China

³³ Liaoning University, Shenyang 110036, People's Republic of China

³⁴ Nanjing Normal University, Nanjing 210023, People's Republic of China

³⁵ Nanjing University, Nanjing 210093, People's Republic of China

³⁶ Nankai University, Tianjin 300071, People's Republic of China

³⁷ North China Electric Power University, Beijing 102206, People's Republic of China

³⁸ Peking University, Beijing 100871, People's Republic of China

³⁹ Qufu Normal University, Qufu 273165, People's Republic of China

- ⁴⁰ Shandong Normal University, Jinan 250014, People's Republic of China
⁴¹ Shandong University, Jinan 250100, People's Republic of China
⁴² Shanghai Jiao Tong University, Shanghai 200240, People's Republic of China
⁴³ Shanxi Normal University, Linfen 041004, People's Republic of China
⁴⁴ Shanxi University, Taiyuan 030006, People's Republic of China
⁴⁵ Sichuan University, Chengdu 610064, People's Republic of China
⁴⁶ Soochow University, Suzhou 215006, People's Republic of China
⁴⁷ South China Normal University, Guangzhou 510006, People's Republic of China
⁴⁸ Southeast University, Nanjing 211100, People's Republic of China
⁴⁹ State Key Laboratory of Particle Detection and Electronics, Beijing 100049, Hefei 230026, People's Republic of China
⁵⁰ Sun Yat-Sen University, Guangzhou 510275, People's Republic of China
⁵¹ Suranaree University of Technology, University Avenue 111, Nakhon Ratchasima 30000, Thailand
⁵² Tsinghua University, Beijing 100084, People's Republic of China
⁵³ (A)Ankara University, 06100 Tandogan, Ankara, Turkey; (B)Istanbul Bilgi University, 34060 Eyup, Istanbul, Turkey; (C)Uludag University, 16059 Bursa, Turkey; (D)Near East University, Nicosia, North Cyprus, Mersin 10, Turkey
⁵⁴ University of Chinese Academy of Sciences, Beijing 100049, People's Republic of China
⁵⁵ University of Groningen, NL-9747 AA Groningen, The Netherlands
⁵⁶ University of Hawaii, Honolulu, Hawaii 96822, USA
⁵⁷ University of Jinan, Jinan 250022, People's Republic of China
⁵⁸ University of Manchester, Oxford Road, Manchester, M13 9PL, United Kingdom
⁵⁹ University of Minnesota, Minneapolis, Minnesota 55455, USA
⁶⁰ University of Muenster, Wilhelm-Klemm-Str. 9, 48149 Muenster, Germany
⁶¹ University of Oxford, Keble Rd, Oxford, UK OX13RH
⁶² University of Science and Technology Liaoning, Anshan 114051, People's Republic of China
⁶³ University of Science and Technology of China, Hefei 230026, People's Republic of China
⁶⁴ University of South China, Hengyang 421001, People's Republic of China
⁶⁵ University of the Punjab, Lahore-54590, Pakistan
⁶⁶ (A)University of Turin, I-10125, Turin, Italy; (B)University of Eastern Piedmont, I-15121, Alessandria, Italy; (C)INFN, I-10125, Turin, Italy
⁶⁷ Uppsala University, Box 516, SE-75120 Uppsala, Sweden
⁶⁸ Wuhan University, Wuhan 430072, People's Republic of China
⁶⁹ Xinyang Normal University, Xinyang 464000, People's Republic of China
⁷⁰ Zhejiang University, Hangzhou 310027, People's Republic of China
⁷¹ Zhengzhou University, Zhengzhou 450001, People's Republic of China
- ^a Also at Bogazici University, 34342 Istanbul, Turkey
^b Also at the Moscow Institute of Physics and Technology, Moscow 141700, Russia
^c Also at the Novosibirsk State University, Novosibirsk, 630090, Russia
^d Also at the NRC "Kurchatov Institute", PNPI, 188300, Gatchina, Russia
^e Also at Istanbul Arel University, 34295 Istanbul, Turkey
^f Also at Goethe University Frankfurt, 60323 Frankfurt am Main, Germany
- ^g Also at Key Laboratory for Particle Physics, Astrophysics and Cosmology, Ministry of Education; Shanghai Key Laboratory for Particle Physics and Cosmology; Institute of Nuclear and Particle Physics, Shanghai 200240, People's Republic of China
^h Also at Key Laboratory of Nuclear Physics and Ion-beam Application (MOE) and Institute of Modern Physics, Fudan University, Shanghai 200443, People's Republic of China
ⁱ Also at Harvard University, Department of Physics, Cambridge, MA, 02138, USA
^j Currently at: Institute of Physics and Technology, Peace Ave.54B, Ulaanbaatar 13330, Mongolia
^k Also at State Key Laboratory of Nuclear Physics and Technology, Peking University, Beijing 100871, People's Republic of China
^l School of Physics and Electronics, Hunan University, Changsha 410082, China
^m Also at Guangdong Provincial Key Laboratory of Nuclear Science, Institute of Quantum Matter, South China Normal University, Guangzhou 510006, China

(Dated: August 18, 2024)

We report new measurements of the branching fraction $\mathcal{B}(D_s^+ \rightarrow \ell^+ \nu)$, where ℓ^+ is either μ^+ or τ^+ ($\rightarrow \pi^+ \bar{\nu}_\tau$), based on 6.32 fb^{-1} of electron-positron annihilation data collected by the BESIII experiment at six center-of-mass energy points between 4.178 and 4.226 GeV. Simultaneously floating the $D_s^+ \rightarrow \mu^+ \nu_\mu$ and $D_s^+ \rightarrow \tau^+ \nu_\tau$ components yields $\mathcal{B}(D_s^+ \rightarrow \tau^+ \nu_\tau) = (5.21 \pm 0.25 \pm 0.17) \times 10^{-2}$, $\mathcal{B}(D_s^+ \rightarrow \mu^+ \nu_\mu) = (5.35 \pm 0.13 \pm 0.16) \times 10^{-3}$, and the ratio of decay widths $R = \frac{\Gamma(D_s^+ \rightarrow \tau^+ \nu_\tau)}{\Gamma(D_s^+ \rightarrow \mu^+ \nu_\mu)} = 9.73_{-0.58}^{+0.61} \pm 0.36$, where the first uncertainties are statistical and the second systematic. No evidence of CP asymmetry is observed in the decay rates $D_s^\pm \rightarrow \mu^\pm \nu_\mu$ and $D_s^\pm \rightarrow \tau^\pm \nu_\tau$: $A_{CP}(\mu^\pm \nu) = (-1.2 \pm 2.5 \pm 1.0)\%$ and $A_{CP}(\tau^\pm \nu) = (+2.9 \pm 4.8 \pm 1.0)\%$. Constraining our measurement to the Standard Model expectation of lepton universality ($R = 9.75$), we find the more precise results

$\mathcal{B}(D_s^+ \rightarrow \tau^+ \nu_\tau) = (5.22 \pm 0.10 \pm 0.14) \times 10^{-2}$ and $A_{CP}(\tau^\pm \nu_\tau) = (-0.1 \pm 1.9 \pm 1.0)\%$. Combining our results with inputs external to our analysis, we determine the $c \rightarrow \bar{s}$ quark mixing matrix element, D_s^+ decay constant, and ratio of the decay constants to be $|V_{cs}| = 0.973 \pm 0.009 \pm 0.014$, $f_{D_s^+} = 249.9 \pm 2.4 \pm 3.5$ MeV, and $f_{D_s^+}/f_{D^+} = 1.232 \pm 0.035$, respectively.

I. INTRODUCTION

Purely leptonic decays of heavy mesons are the subject of great experimental and theoretical interest because of their potential for precise tests of the Standard Model (SM), including determination of the Cabibbo-Kobayashi-Maskawa (CKM) matrix elements and sensitivity to non-SM physics. Leptonic decays of charmed mesons play an important role in this, with clean experimental signatures and the opportunity for rigorous tests of strong-interaction theory, especially lattice-QCD (LQCD) calculations. In the decay process $D_s^+ \rightarrow \ell^+ \nu_\ell$, the charm quark (c) and antistrange quark (\bar{s}) annihilate through a virtual W boson to a charged and neutral lepton pair. (Throughout this article, charge conjugate modes are implied unless otherwise noted.) According to the SM, the branching fraction for this process (ignoring radiative corrections) is given as follows:

$$\mathcal{B}(D_s^+ \rightarrow \ell^+ \nu_\ell) = \tau_{D_s^+} \frac{G_F^2}{8\pi} f_{D_s^+}^2 m_\ell^2 m_{D_s^+} \left(1 - \frac{m_\ell^2}{m_{D_s^+}^2}\right)^2 |V_{cs}|^2, \quad (1)$$

where $\tau_{D_s^+}$ is the D_s^+ lifetime, $m_{D_s^+}$ is the mass of D_s^+ , m_ℓ is the mass of the charged lepton (e^+ , μ^+ , or τ^+), and G_F is the Fermi coupling constant, all of which are known to precision [1]. The remaining two factors, $|V_{cs}|$ and $f_{D_s^+}$, must be determined experimentally and are of great interest. (1) V_{cs} is a fundamental SM parameter, the CKM matrix element describing the coupling between the c and \bar{s} quarks. (2) $f_{D_s^+}$ is the D_s^+ decay constant, the amplitude for quark-antiquark annihilation inside the meson, which can be thought of as the overlap of the wave functions of c and \bar{s} at zero spatial separation.

It follows from Eq. (1) that measurement of the branching fraction $\mathcal{B}(D_s^+ \rightarrow \ell^+ \nu_\ell)$ is essentially a determination of $f_{D_s^+}^2 |V_{cs}|^2$. In practice, we can determine $f_{D_s^+}$ by combining a measurement of $\mathcal{B}(D_s^+ \rightarrow \ell^+ \nu_\ell)$ with an independent determination of $|V_{cs}|$, thereby testing theoretical predictions, primarily from LQCD. Testing the LQCD calculations in D and D_s^+ decays is especially important to validate their application to the B -meson sector, in which the precision of experimental determination of f_{B^+} is very limited due to the small value of $|V_{ub}|$, $0.00361^{+0.00011}_{-0.00009}$ [1]. It is also possible to reverse this approach, determining $|V_{cs}|$ from $\mathcal{B}(D_s^+ \rightarrow \ell^+ \nu_\ell)$ with a theoretical estimate of $f_{D_s^+}$ from LQCD and comparing the result with other experimental determinations of $|V_{cs}|$.

The ratio of decay widths for leptonic decays to μ and

τ is also an interesting quantity to measure:

$$R = \frac{\Gamma(D_s^+ \rightarrow \tau^+ \nu_\tau)}{\Gamma(D_s^+ \rightarrow \mu^+ \nu_\mu)} = \frac{m_\tau^2 (1 - \frac{m_\tau^2}{m_{D_s^+}^2})^2}{m_\mu^2 (1 - \frac{m_\mu^2}{m_{D_s^+}^2})^2}. \quad (2)$$

In this ratio, the decay constant and the CKM element cancel, giving a very precise SM prediction of $R = 9.75 \pm 0.01$. Any deviation from this value potentially indicates the existence of non-SM physics.

Using the known values of the lepton masses and other constants [1], the measured D_s^+ lifetime [1] (including recent improvements in precision by the LHCb Collaboration [2]), the weighted average of recent four-flavor LQCD calculations [3] ($f_{D_s^+} = 249.9 \pm 0.5$ MeV), and the latest determination of the $c \rightarrow \bar{s}$ coupling from the global fit of CKM parameters [1] ($|V_{cs}| = 0.97320 \pm 0.00011$), one arrives at the following SM predictions of the D_s^+ leptonic branching fractions: $\mathcal{B}(D_s^+ \rightarrow e^+ \nu_e) = (1.261 \pm 0.004) \times 10^{-7}$, $\mathcal{B}(D_s^+ \rightarrow \mu^+ \nu_\mu) = (5.360 \pm 0.017) \times 10^{-3}$, and $\mathcal{B}(D_s^+ \rightarrow \tau^+ \nu_\tau) = (5.221 \pm 0.018)\%$. In this article, we report new measurements of the branching fractions $\mathcal{B}(D_s^+ \rightarrow \mu^+ \nu_\mu)$ and $\mathcal{B}(D_s^+ \rightarrow \tau^+ \nu_\tau)$ (via $\tau^+ \rightarrow \pi^+ \bar{\nu}_\tau$), and of the CP -violating asymmetries $A_{CP}(\ell^\pm \nu_\ell)$. These measurements have been made with 6.32 fb^{-1} of e^+e^- annihilation data collected at center-of-mass energies between 4178 and 4226 MeV with the BESIII detector [4] at the Beijing Electron Positron Collider (BEPCII) [5]. This work, which uses a larger data sample and a procedure that is simultaneously sensitive to both $D_s^+ \rightarrow \mu^+ \nu_\mu$ and $D_s^+ \rightarrow \tau^+ \nu_\tau$ decays, is distinct from and supersedes our previous measurement of $\mathcal{B}(D_s^+ \rightarrow \mu^+ \nu_\mu)$ [6].

II. THE BESIII EXPERIMENT AND DATA SETS

BESIII [4] is a cylindrical spectrometer with a geometrical acceptance of 93% of 4π . It consists of a small-celled, helium-based main drift chamber (MDC), a plastic scintillator time-of-flight system (TOF), a CsI(Tl) electromagnetic calorimeter (EMC), a superconducting solenoid providing a 1.0-T magnetic field, and a muon counter (MUC). The charged particle momentum resolution is 0.5% at a transverse momentum of 1 GeV/ c . The specific ionization (dE/dx) measurement provided by the MDC has a resolution of 6%, and provides 3σ separation of charged pions and kaons. The time resolution of the TOF is 80 ps (110 ps) in the central barrel (end-cap) region of the detector. The end-cap TOF system was upgraded with multigap resistive plate chamber technology in 2015 [7], improving its time resolution to 60 ps. Approximately 83% of the sample employed in this work

was taken with the improved configuration. The energy resolution for photons is 2.5% (5%) at 1 GeV in the barrel (end-cap) region of the EMC. A more detailed description of the BESIII detector is given in Ref. [4].

The data samples employed in this work were taken at six e^+e^- center-of-mass energies ($E_{\text{cm}} = 4178, 4189, 4199, 4209, 4219,$ and around 4226 MeV [8]). The integrated luminosities for these subsamples are 3189.0, 526.7, 526.0, 517.1, 514.6, and 1047.3 pb^{-1} [9], respectively. For simplicity, we refer to these datasets as 4180, 4190, 4200, 4210, 4220, and 4230 in the rest of this article. For some aspects of our analysis, especially in assessing systematic uncertainties, we organize the samples into three groups that were acquired during the same year under consistent running conditions. The 4180 sample was taken in 2016, while the group 4190-4220 was taken in 2017 and 4230 was taken in 2013.

To assess background processes and determine detection efficiencies, we produce and analyze GEANT4-based [10] Monte Carlo (MC) simulation samples for all six datasets, with sizes that are 40 times the integrated luminosity of data (“40 \times ”). The MC samples are produced using known decay rates [1] and correct angular distributions by two event generators, EVTGEN [11] for charm and charmonium decays and KKMC [12] for continuum processes. The samples consist of $e^+e^- \rightarrow D\bar{D}, D^*D, D^*D^*, D_sD_s, D_s^*D_s, D_s^*D_s^*, DD^*\pi, DD\pi, q\bar{q}(q = u, d, s), \gamma J/\psi, \gamma\psi(3686),$ and $\tau^+\tau^-$. Charmonium decays that are not accounted for by exclusive measurements are simulated by LUNDCHARM [13]. Additionally we generate separate samples consisting only of signal events, with size 300 times larger than is expected in our data. All MC simulations include the effects of initial-state radiation (ISR) and final-state radiation (FSR). We simulate ISR with CONEXC [14] for $e^+e^- \rightarrow c\bar{c}$ events within the framework of EvtGen, and with KKMC for noncharm continuum processes. FSR is simulated with PHOTOS [15].

III. ANALYSIS METHOD

We employ the double-tag technique pioneered by the MARK III Collaboration [16] in our selection of $D_s^\pm \rightarrow \ell^\pm \nu_\ell$ decays in $e^+e^- \rightarrow D_s^{*\pm} D_s^\mp$ events. In this method, a D_s^- is fully reconstructed through one of several hadronic decay modes (tag side), while we reconstruct only one charged track from the D_s^+ (signal side). Note that the reconstructed tag-side D_s can either be directly produced from the e^+e^- collision (direct) or be the daughter of a D_s^* (indirect). We reconstruct the radiative photon from $D_s^* \rightarrow \gamma D_s$ in the tag-side selection and use it in the analysis of the signal side. (Further explanation is provided in Sec. III A.) The absolute branching fraction determined by this method does not depend on the integrated lumi-

nosity or the produced number of $D_s^{*\pm} D_s^\mp$ pairs:

$$\mathcal{B}(D_s^+ \rightarrow \mu^+ \nu_\mu) = \frac{N_{DT}^{\mu\nu}}{\sum_i N_{ST}^i (\epsilon_{DT}^{\mu\nu,i} / \epsilon_{ST}^i)}, \quad (3)$$

where $N_{DT} = \sum_i N_{DT}^i$ is the summed yield over tag modes of double-tag (DT) events in which the tag side and signal side are simultaneously reconstructed, N_{ST}^i is the single-tag (ST) yield of reconstructed D_s^- for tag mode i , and $\epsilon_{DT}^{\mu\nu,i}$ and ϵ_{ST}^i are the corresponding reconstruction efficiencies. Similarly for $\mathcal{B}(D_s^+ \rightarrow \tau^+ \nu_\tau)$ we have

$$\mathcal{B}(D_s^+ \rightarrow \tau^+ \nu_\mu) = \frac{N_{DT}^{\tau\nu}}{\sum_i N_{ST}^i (\epsilon_{DT}^{\tau\nu,i} / \epsilon_{ST}^i) \mathcal{B}(\tau^+ \rightarrow \pi^+ \bar{\nu}_\tau)}, \quad (4)$$

where $\epsilon_{DT}^{\tau\nu,i}$ does not include $\mathcal{B}(\tau^+ \rightarrow \pi^+ \bar{\nu}_\tau)$ but $\epsilon_{DT}^{\ell\nu,i}$ does include $\mathcal{B}(D_s^* \rightarrow \gamma D_s)$.

In the ratios of $N_{DT}^{\ell\nu} / N_{ST}^i$ and $\epsilon_{DT}^{\ell\nu,i} / \epsilon_{ST}^i$, systematic uncertainty associated with the tag-side analysis mostly cancels, except for a possible uncertainty due to variations in ST reconstruction efficiencies (tag bias, discussed in Sec. IV A).

A. Selection of tagged D_s^- candidates

The ST D_s^- is reconstructed using tracks and EMC showers that pass several quality requirements. The selection criteria for D_s^- daughters and the reconstruction procedures are the same as those described in Ref. [17]. Tracks must be within the fiducial region ($|\cos\theta| < 0.93$, where θ is the polar angle relative to the positron beam direction) and originate within 1 cm (10 cm) of the interaction point in the plane transverse to the beam direction (along the beam direction). This requirement on the primary vertex is not applied for the reconstruction of $K_S^0 \rightarrow \pi^+\pi^-$, for which we constrain the charged pion pair to have a common vertex with a loose fit-quality requirement of $\chi^2 < 100$ for 1 degree of freedom. To be selected as a photon candidate, an EMC shower must not be associated with any charged track [18], must have an EMC hit time between 0 and 700 ns to suppress activity that is not consistent with originating from the collision event, and must have an energy of at least 25 MeV if it is in the barrel region of the detector ($|\cos\theta| < 0.8$) and 50 MeV if it is in the end-cap region ($0.86 < |\cos\theta| < 0.92$) to suppress noise in the EMC.

We apply K/π particle identification (PID) based on TOF and dE/dx measurements, with the identity as a pion or kaon assigned based on which hypothesis has the higher likelihood. Pions from the intermediate states $K_S^0 \rightarrow \pi^+\pi^-$, $\eta \rightarrow \pi^+\pi^-\pi^0$ and $\eta' \rightarrow \pi^+\pi^-\eta$ are not required to satisfy the K/π -identification requirement. We also require that the reconstructed momentum for any charged or neutral pion have a magnitude of at least 100 MeV/ c to suppress events from $D^* \rightarrow D\pi$.

We select tag modes for this analysis to maximize signal sensitivity and minimize tag bias by performing the entire analysis procedure on our cocktail MC sample with various combinations of tag modes. The following thirteen D_s^- hadronic decay modes are used: $D_s^- \rightarrow K_S^0 K^-$, $K^- K^+ \pi^-$, $K_S^0 K^- \pi^0$, $K^- K^+ \pi^- \pi^0$, $K_S^0 K^- \pi^+ \pi^-$, $K_S^0 K^+ \pi^- \pi^-$, $\pi^- \pi^- \pi^+$, $\pi^- \eta$, $\rho^- \eta$, $\rho^- \eta_{3\pi}$, $\pi^- \eta'_{\pi\pi\eta}$, $\pi^- \eta'_{\gamma\rho}$, and $K^- \pi^- \pi^+$, where $\pi^0 \rightarrow \gamma\gamma$, $K_S^0 \rightarrow \pi^+ \pi^-$, $\eta \rightarrow \gamma\gamma$, $\eta_{3\pi} \rightarrow \pi^+ \pi^- \pi^0$, $\rho^{-(0)} \rightarrow \pi^{0(+)} \pi^-$, $\eta'_{\pi\pi\eta} \rightarrow \pi^+ \pi^- \eta$, and $\eta'_{\gamma\rho} \rightarrow \gamma\rho^0$. Requirements on invariant-mass ranges for the intermediate states π^0 , K_S^0 , η , $\eta_{3\pi}$, ρ , $\eta'_{\pi\pi\eta}$, and $\eta'_{\gamma\rho}$ are chosen to cover $\pm(3-4)\sigma$ of the signal mass resolutions, with the exception of ρ , for which $520 (500) < M_{\pi\pi} < 1000 \text{ MeV}/c^2$ is selected for the charged (neutral) case. We also require an isolation criterion for photons used in the reconstruction of $\eta' \rightarrow \gamma\rho^0$; the reconstructed photons must be separated from the extrapolated positions of all charged particles by more than 20° . For the decay mode $D_s^- \rightarrow K^- \pi^- \pi^+$ we exclude the dipion mass range $486 < M_{\pi\pi} < 510 \text{ MeV}/c^2$ to avoid overlap with the $D_s^- \rightarrow K_S^0 K^-$ mode.

Once the tag-side D_s^- is reconstructed, we preselect our sample by requiring that the invariant mass of the reconstructed D_s^- satisfy the condition $1900 < M_{\text{inv}}(D_s^-) < 2030 \text{ MeV}/c^2$. Then we calculate the recoil mass against the D_s^- tag inclusively as $M_{\text{rec}}^2 c^4 = (E_{\text{cm}} - \sqrt{|\vec{p}_{D_s^-}|^2 c^2 + m_{D_s^-}^2 c^4})^2 - |\vec{p}_{D_s^-}|^2 c^2$ in the center-of-mass system of the initial e^+e^- , where $E_{\text{cm}} = 2 \times E_{\text{beam}}$, $\vec{p}_{D_s^-}$ is the three-momentum of the reconstructed D_s^- , and $m_{D_s^-}$ is the known D_s mass [1]. Figure 1 shows the distribution of recoil mass against $D_s^- \rightarrow K^- K^+ \pi^-$ tags in the 4180 dataset. All $e^+e^- \rightarrow D_s^{*\pm} D_s^\mp$ events accumulate near $m_{D_s^*} = 2112.2 \text{ MeV}/c^2$ [1], with the direct component populating the central peak and the indirect component distributed more broadly. We require

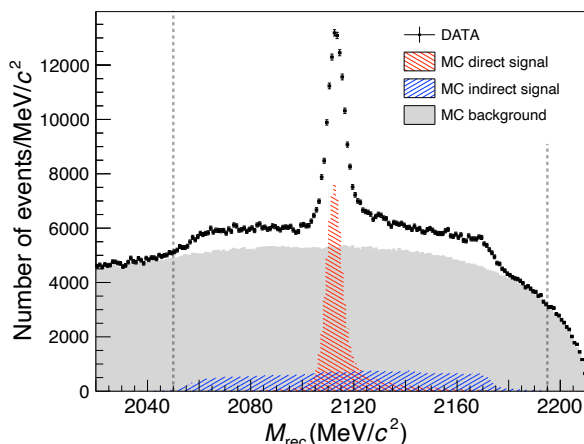


FIG. 1. Recoil mass distributions against $D_s^- \rightarrow K^- K^+ \pi^-$ for 4180 data and MC-simulated background, which mostly consists of charm decays and continuum processes.

$2050 < M_{\text{rec}} < 2195 \text{ MeV}/c^2$ for the 4180 data to en-

sure that events are consistent with $e^+e^- \rightarrow D_s^{*\pm} D_s^\mp$. For other data samples taken at higher E_{cm} , the tails of the indirect D_s events extend more widely. We expand the selected M_{rec} range to maintain roughly constant $KK\pi$ tag efficiencies for different values of E_{cm} , except for the 4230 data, whose energy is above the threshold for production of $D_s^* D_s^*$. In this case we require $2040 < M_{\text{rec}} < 2220 \text{ MeV}/c^2$ to suppress D_s from $D_s^* D_s^*$ events, which mostly have $M_{\text{rec}} > 2230 \text{ MeV}/c^2$.

When multiple reconstructed candidates are found for a given D_s tag mode and electric charge, we keep only the one with the best $D_s^* \rightarrow \gamma D_s$ photon candidate. In the D_s^* rest frame, the emitted photon energy is monochromatic, with energy $(m_{D_s^*}^2 c^4 - m_{D_s}^2 c^4)/(2m_{D_s^*} c^2) = 138.9 \text{ MeV}$. Once the tag-side D_s^- is reconstructed, we loop over the remaining photon candidates to construct the four-momentum of the D_s^* candidate based on two hypotheses. For the first hypothesis, we assume that the tag is direct, the photon is on the signal side, and $p(D_s^{*+}) = p_{e^+e^-} - p_{\text{tag}}$. For the second, we assume that the tag is indirect, the photon is on the tag side, and $p(D_s^{*-}) = p_\gamma + p_{\text{tag}}$. We then choose between these the combination that gives E_γ closest to 138.9 MeV in the D_s^* rest frame and use this in the rest of our analysis. Additionally, we require $119 < E_\gamma < 149 \text{ MeV}$ to suppress backgrounds further. This range is selected based on MC studies of the signal side, as is described in Sec. III B. The resulting optimized photon selection efficiency is $\sim 90\%$. While we do not use information about the transition photon in determining the tag-side yields, we perform the photon reconstruction and apply the additional selection on E_γ at this point to minimize the systematic uncertainty due to the best-tag selection. The effect on the signal efficiency of selecting the transition photon is minimal due to the simple decay topology of the signal side, with only one charged track.

To determine the tag yields, we perform an unbinned maximum likelihood fit to $M_{\text{inv}}(D_s^-)$ in the range $1900 < M_{\text{inv}}(D_s^-) < 2030 \text{ MeV}/c^2$. The signal functions are based on distributions from MC simulations, obtained by the Gaussian kernel estimation method [19], and convolved with a Gaussian function to account for differing resolution between data and MC samples. In practice it is difficult to float the width of the Gaussian function in fits for tag modes with larger backgrounds in smaller samples (e.g., 4220 data). Because of this, we assume that the relative difference between data and MC samples is consistent among the different datasets and simultaneously fit to all six samples, sharing a single convolved Gaussian function for a given tag mode. We estimate possible systematic uncertainty associated with this assumption in Sec. IV B.

Backgrounds in the invariant-mass fits are represented by low-degree Chebyshev polynomials (first to third, depending on the tag mode). Figure 2 shows fits to the $M_{\text{inv}}(D_s^-)$ distributions of the thirteen tag modes for the 4180 dataset. In the fits of tag modes $D_s^- \rightarrow K_S^0 K^-$ and $D_s^- \rightarrow K^- K^+ \pi^-$ MC simulations predict small peaking

backgrounds from $D^- \rightarrow K_S^0 \pi^-$ and $D^- \rightarrow K^+ \pi^- \pi^-$, which are taken into account in the fits. Table I shows the ST efficiencies, ϵ_{ST} . The corresponding ST yields from data are also shown in Table II.

B. Selection of $D_s^+ \rightarrow \ell^+ \nu_\ell$ events

True $D_s^+ \rightarrow \ell^+ \nu_\ell$ signal events include either $D_s^+ \rightarrow \mu^+ \nu_\mu$ or $D_s^+ \rightarrow \tau^+ (\rightarrow \pi^+ \bar{\nu}_\tau) \nu_\tau$ accompanying a D_s^- hadronic tag. Signal selection begins with the requirement that there be only one additional track that is unused in the reconstruction of the tag ($N_{tk} = 1$). The corresponding particle must have electric charge opposite to the tag and satisfy the pion PID criteria described in Sec. III A. (The pion PID response closely approximates that for a muon because pions and muons are charged particles with similar masses.) It is significant that the systematic uncertainty arising from the PID requirement in the signal selection does not cancel, as it does for tag reconstruction. We study control samples of $D_s^- \rightarrow K^- K^+ \pi^-$, $D^0 \rightarrow K^- \pi^+$ and $D^0 \rightarrow K^- \pi^- \pi^+ \pi^+$ for all datasets and observe differences in PID efficiencies between data and MC samples of about 1%. Here the D^0 sample is obtained via $e^+ e^- \rightarrow D^{*+} (\rightarrow \pi^+ D^0) D^{(*)-}$. Corrections are applied to MC-determined efficiencies.

We split the signal-track sample into two parts based on the energy-deposit properties of muons and pions in the EMC, as was done previously in similar analyses [20, 21]. Candidates with signal-track energy deposit satisfying $E_{\text{EMC}} \leq 300$ MeV are classified as μ -like and the remainder as π -like. Based on MC simulation, we estimate that the μ -like sample includes $\sim 99\%$ of $D_s^+ \rightarrow \mu^+ \nu_\mu$ events and $\sim 58\%$ of $D_s^+ \rightarrow \tau^+ (\rightarrow \pi^+ \bar{\nu}_\tau) \nu_\tau$ events.

As mentioned in Sec. III A, we impose the additional requirement on signal candidates from $D_s^* \rightarrow \gamma D_s$ that the selected photon have an energy in the D_s^* rest frame that satisfies $119 < E_\gamma < 149$ MeV. This criterion is optimized based on a detailed MC study. Distributions of E_γ for MC and data are shown in Fig. 3. Here the input $\mathcal{B}(D_s^+ \rightarrow \mu^+ \nu_\mu)$ and $\mathcal{B}(D_s^+ \rightarrow \tau^+ \nu_\tau)$ in our MC samples are 5.38×10^{-3} and 5.54×10^{-2} , respectively.

We suppress candidate signal events that are not true $D_s^+ \rightarrow \ell^+ \nu_\ell$ by considering three additional variables that are sensitive to unreconstructed particles. The first is $\cos \theta_{\text{miss}}$, where θ_{miss} is the polar angle of $\vec{p}_{\text{miss}} = -\vec{p}_{\text{tag}} - \vec{p}_\gamma - \vec{p}_{\mu/\pi}$ in the $e^+ e^-$ center-of-mass frame. We require $|\cos \theta_{\text{miss}}| < 0.9$ to ensure that \vec{p}_{miss} points into the fiducial volume of our detector. The second variable is ANG , the opening angle between \vec{p}_{miss} and the most energetic unused EMC shower. Events with a K_L^0 or an energetically asymmetric decay from $\pi^0 \rightarrow \gamma\gamma$ or $\eta \rightarrow \gamma\gamma$ tend to leave detectable EMC energy deposits near the \vec{p}_{miss} direction. We require $ANG > 40^\circ$ to suppress such events. The third variable is $E_{\text{neu}}^{\text{max}}$, the maximum unused EMC shower energy. Requiring $E_{\text{neu}}^{\text{max}} < 300$ MeV helps to ensure that nothing energetic is unaccounted for in

selected events.

C. Fit

1. Fitting to simulated samples

We infer the presence of neutrinos in the final states from the event missing mass-squared, $M_{\text{miss}}^2 = E_{\text{miss}}^2 - |\vec{p}_{\text{miss}} c|^2$, where $E_{\text{miss}} = E_{\text{cm}} - \sqrt{|\vec{p}_{\text{tag}} c|^2 + m_{D_s}^2} c^4 - E_\gamma - E_{\mu/\pi}$ is computed in the $e^+ e^-$ center-of-mass frame, and m_{D_s} is fixed to the known value [1]. We determine the $\mathcal{B}(D_s^+ \rightarrow \ell^+ \nu)$ signal yields with a simultaneous unbinned maximum likelihood fit to the two-dimensional distributions of the tag-side invariant mass $M_{\text{inv}}(D_s^-)$ versus M_{miss}^2 for the six E_{cm} samples. The fit range on the $M_{\text{inv}}(D_s^-)$ axis is the same as we use to fit to the tag-side D_s^- , $1900 < M_{\text{inv}}(D_s^-) < 2030$ MeV/ c^2 , while we choose $-0.2 < M_{\text{miss}}^2 < 0.2$ (GeV/ c^2) 2 on the other axis to avoid peaking backgrounds in $M_{\text{miss}}^2 > 0.2$ (GeV/ c^2) 2 coming from $D_s^+ \rightarrow K^0 \pi^+$ when the K^0 is undetected.

Background processes contributing $D_s^+ \rightarrow \ell^+ \nu_\ell$ candidate signal events can be classified in five major categories. (1) The tag-side D_s^- is misreconstructed, but everything else is correct, producing smooth distributions in M_{inv} , but peaks in M_{miss}^2 . (2) The photon from $D_s^* \rightarrow \gamma D_s$ is misreconstructed, but everything else is correct, leading to peaking sharply in M_{inv} and broadly in M_{miss}^2 . (3) The signal-side track is not from $D_s^+ \rightarrow (\mu^+/\tau^+) \nu$, but everything else is correct, giving peaks in M_{inv} and smooth distributions in M_{miss}^2 . (4) The reconstructed track is from $D_s^+ \rightarrow \tau^+ \nu_\tau$, but not from $\tau^+ \rightarrow \pi^+ \bar{\nu}_\tau$, and everything else is correct, with peaks in M_{inv} but smooth distributions in M_{miss}^2 . (Note that, while such events are not analyzed correctly, they are not background and we float this contribution with the $\tau^+ \rightarrow \pi^+ \bar{\nu}_\tau$ signal.) (5) All remaining background, both charm and noncharm, which has a smooth continuous shape. Two-dimensional background distributions for fitting are constructed based on products of one-dimensional probability distribution functions (PDFs) for $M_{\text{inv}}(D_s^-)$ and M_{miss}^2 .

Fits are performed with MC-based shapes for signals, similarly extracted by the kernel estimation method [19], and the following distributions for the five background components. (1) Wrong tag: first-order Chebyshev polynomial for $M_{\text{inv}}(D_s^-)$ and an MC-based shape for M_{miss}^2 . (2) Wrong photon: MC-based shapes for both $M_{\text{inv}}(D_s^-)$ and M_{miss}^2 . (3) Wrong track: MC-based shapes for both $M_{\text{inv}}(D_s^-)$ and M_{miss}^2 . (4) τ decays to final states other than $\pi^+ \bar{\nu}_\tau$: MC-based shapes for both $M_{\text{inv}}(D_s^-)$ and M_{miss}^2 . (5) Remainder: first-order Chebyshev polynomial for $M_{\text{inv}}(D_s^-)$ and first-order exponential polynomial ($\propto e^{C \cdot M_{\text{miss}}^2}$) for M_{miss}^2 . To compensate for differences between the simulated detector response and data, each PDF [$M_{\text{inv}}(D_s^-)$ and M_{miss}^2] is convolved with a Gaussian function that is shared over the six data samples, assum-

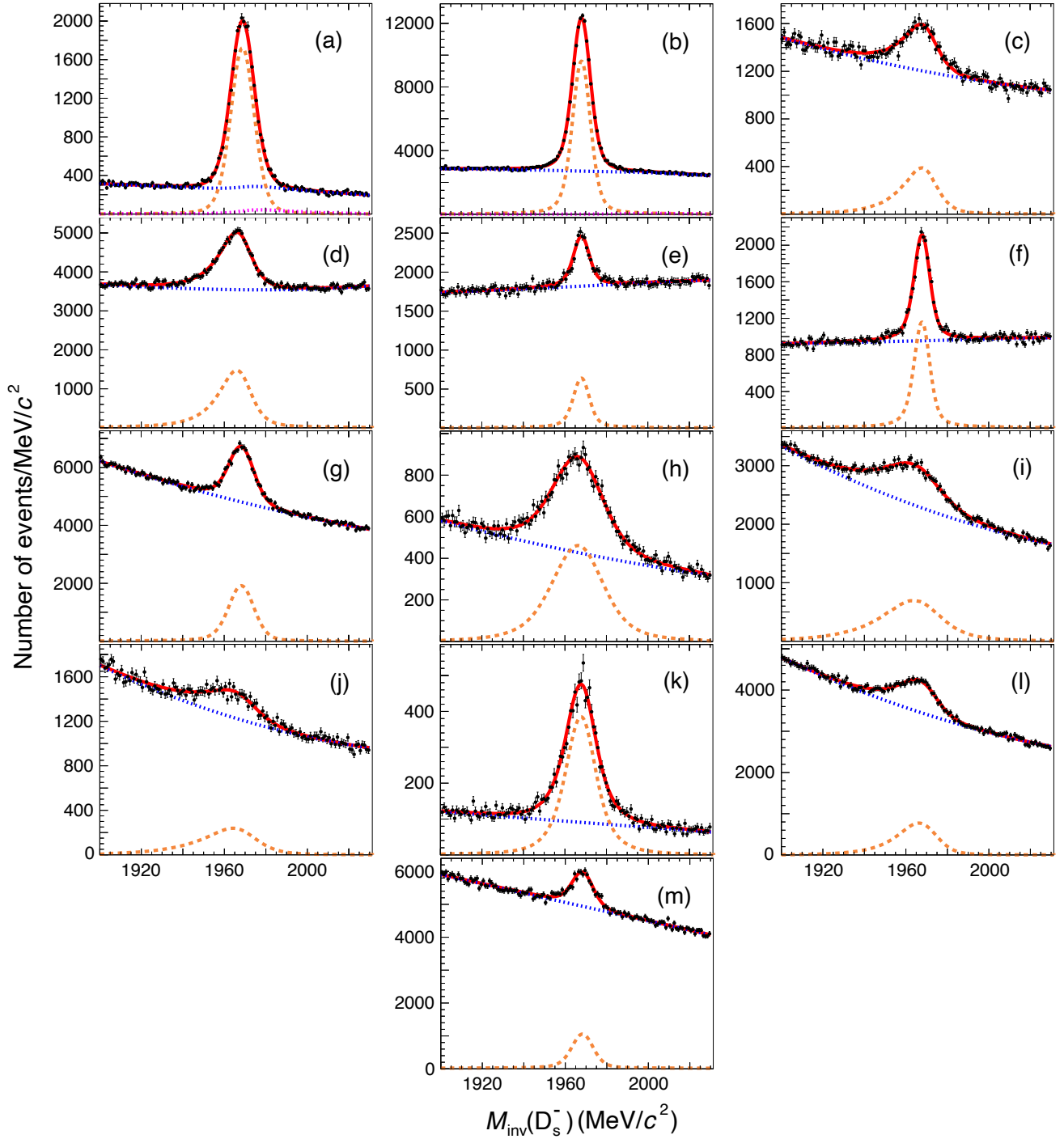


FIG. 2. Fits to D_s^- invariant-mass distributions in the 4180 data for the following thirteen ST decay modes: (a) $K_S^0 K^-$, (b) $K^- K^+ \pi^-$, (c) $K_S^0 K^- \pi^0$, (d) $K^- K^+ \pi^- \pi^0$, (e) $K_S^0 K^- \pi^+ \pi^-$, (f) $K_S^0 K^+ \pi^- \pi^-$, (g) $\pi^- \pi^+ \pi^-$, (h) $\pi^- \eta$, (i) $\rho^- \eta$, (j) $\rho^- \eta_{3\pi}$, (k) $\pi^- \eta'_{\pi\pi\eta}$, (l) $\pi^- \eta'_{\gamma\rho}$, and (m) $K^- \pi^+ \pi^-$. Points are data, while red-solid lines represent the total fits, blue-dotted lines are the fitted background shapes, and the orange-dashed lines correspond to the fitted signal shapes. The magenta-dotted lines only seen in the two tag modes, (a) $K_S^0 K^-$ and (b) $K^- K^+ \pi^-$, are the fitted nonsmooth background shapes representing $D^- \rightarrow K_S^0 \pi^-$ and $D^- \rightarrow K^+ \pi^- \pi^-$, respectively.

TABLE I. ST reconstruction efficiencies (ϵ_{ST} in %) with their statistical uncertainties for the thirteen tag modes and six data samples. Efficiencies do not include the following intermediate-state branching fractions: $K_S^0 \rightarrow \pi^+\pi^-$, $\pi^0 \rightarrow \gamma\gamma$, $\eta \rightarrow \gamma\gamma$, $\eta_{3\pi} \rightarrow \pi^+\pi^-\pi^0$, $\eta'_{\pi\pi\eta} \rightarrow \pi^+\pi^-\eta$, $\eta'_{\gamma\rho} \rightarrow \gamma\rho^0$, and $\rho \rightarrow \pi\pi$.

Tag mode	4180	4190	4200	4210	4220	4230
$K_S^0 K^-$	38.5 ± 0.1	38.1 ± 0.3	38.6 ± 0.3	38.7 ± 0.2	38.3 ± 0.3	39.0 ± 0.3
$K^- K^+ \pi^-$	34.3 ± 0.1	34.1 ± 0.1	34.4 ± 0.1	34.1 ± 0.2	34.4 ± 0.1	34.8 ± 0.1
$K_S^0 K^- \pi^0$	14.3 ± 0.2	14.6 ± 0.5	14.3 ± 0.5	13.8 ± 0.5	13.8 ± 0.6	14.7 ± 0.5
$K^- K^+ \pi^- \pi^0$	9.2 ± 0.1	9.1 ± 0.1	9.2 ± 0.1	9.5 ± 0.1	9.1 ± 0.2	9.5 ± 0.1
$K_S^0 K^- \pi^+ \pi^-$	17.1 ± 0.2	16.9 ± 0.5	16.7 ± 0.5	16.0 ± 0.5	16.6 ± 0.6	17.8 ± 0.5
$K_S^0 K^+ \pi^- \pi^-$	19.0 ± 0.1	18.8 ± 0.2	19.2 ± 0.2	19.1 ± 0.2	18.9 ± 0.3	19.8 ± 0.2
$\pi^- \pi^+ \pi^-$	42.6 ± 0.2	41.7 ± 0.5	42.3 ± 0.6	41.8 ± 0.5	41.8 ± 0.7	43.1 ± 0.6
$\pi^- \eta_{\gamma\gamma}$	35.5 ± 0.2	35.8 ± 0.5	35.5 ± 0.6	33.9 ± 0.6	33.8 ± 0.8	35.7 ± 0.6
$\rho^- \eta_{\gamma\gamma}$	13.6 ± 0.1	13.9 ± 0.3	13.6 ± 0.3	13.4 ± 0.3	13.5 ± 0.4	14.5 ± 0.4
$\rho^- \eta_{3\pi}$	6.1 ± 0.1	5.6 ± 0.4	5.6 ± 0.4	6.3 ± 0.4	5.6 ± 0.5	5.9 ± 0.4
$\pi^- \eta'_{\pi\pi\eta}$	20.3 ± 0.1	19.8 ± 0.2	20.1 ± 0.2	20.0 ± 0.2	20.1 ± 0.3	20.2 ± 0.2
$\pi^- \eta'_{\gamma\rho}$	27.3 ± 0.3	27.5 ± 0.7	26.6 ± 0.8	26.4 ± 0.7	28.3 ± 1.0	28.0 ± 0.8
$K^- \pi^+ \pi^-$	35.9 ± 0.3	35.0 ± 0.8	34.2 ± 0.8	34.0 ± 0.8	33.3 ± 1.0	34.7 ± 0.8

TABLE II. Measured ST yields (N_{ST}) for each tag mode and their sums over tag modes (“SUM”) for each data sample, in units of 10^3 . The uncertainties shown are only statistical.

Tag mode	4180	4190	4200	4210	4220	4230
$K_S^0 K^-$	26.2 ± 0.2	4.1 ± 0.1	4.1 ± 0.1	3.6 ± 0.1	3.0 ± 0.1	5.5 ± 0.1
$K^- K^+ \pi^-$	120.6 ± 0.6	19.0 ± 0.2	18.6 ± 0.2	17.3 ± 0.2	15.1 ± 0.2	25.2 ± 0.2
$K_S^0 K^- \pi^0$	9.7 ± 0.4	1.5 ± 0.2	1.7 ± 0.2	1.3 ± 0.2	0.9 ± 0.2	2.1 ± 0.2
$K^- K^+ \pi^- \pi^0$	35.1 ± 0.8	6.3 ± 0.3	5.6 ± 0.3	5.2 ± 0.3	4.9 ± 0.3	7.5 ± 0.3
$K_S^0 K^- \pi^+ \pi^-$	7.8 ± 0.3	1.2 ± 0.1	1.3 ± 0.1	1.0 ± 0.1	0.9 ± 0.1	1.5 ± 0.1
$K_S^0 K^+ \pi^- \pi^-$	14.0 ± 0.2	2.2 ± 0.1	2.2 ± 0.1	1.9 ± 0.1	1.9 ± 0.1	2.8 ± 0.1
$\pi^- \pi^+ \pi^-$	33.1 ± 0.6	5.4 ± 0.2	5.2 ± 0.2	4.3 ± 0.2	3.8 ± 0.2	6.7 ± 0.3
$\pi^- \eta_{\gamma\gamma}$	16.0 ± 0.5	2.4 ± 0.2	2.4 ± 0.2	2.4 ± 0.2	2.0 ± 0.2	3.2 ± 0.2
$\rho^- \eta_{\gamma\gamma}$	28.5 ± 0.9	3.9 ± 0.4	4.5 ± 0.4	4.3 ± 0.4	3.5 ± 0.4	6.1 ± 0.5
$\rho^- \eta_{3\pi}$	8.6 ± 0.6	1.4 ± 0.2	1.2 ± 0.2	1.1 ± 0.2	0.7 ± 0.2	2.1 ± 0.4
$\pi^- \eta'_{\pi\pi\eta}$	8.4 ± 0.1	1.4 ± 0.1	1.3 ± 0.1	1.2 ± 0.1	1.0 ± 0.1	1.7 ± 0.1
$\pi^- \eta'_{\gamma\rho}$	20.8 ± 0.8	3.3 ± 0.3	3.2 ± 0.3	3.0 ± 0.3	2.5 ± 0.3	4.7 ± 0.4
$K^- \pi^+ \pi^-$	16.0 ± 0.5	2.6 ± 0.2	2.3 ± 0.2	2.3 ± 0.2	1.7 ± 0.2	3.4 ± 0.2
SUM	344.8 ± 2.0	54.7 ± 0.7	53.8 ± 0.8	48.8 ± 0.8	42.1 ± 0.7	72.5 ± 1.0

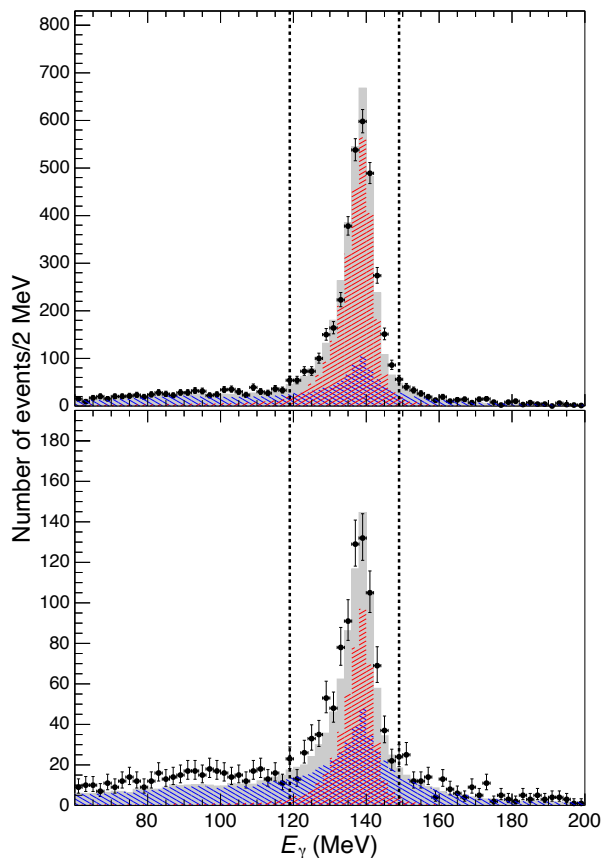


FIG. 3. E_γ spectra in the D_s^* rest frame for μ -like (top) and π -like (bottom) samples summed over the six E_{cm} values (weighted by integrated luminosity). The gray-shaded histograms represent the scaled $40\times$ MC predictions, while the crosshatched histograms show the signals (red, bottom-left to top-right) and the backgrounds (blue, top-left to bottom-right). The black points with error bars are the corresponding measurements from data, and the dashed vertical lines show our nominal selection requirement of $119 < E_\gamma < 149$ MeV.

ing that the data/MC differences do not depend on E_{cm} and running conditions.

Normalizations of the five background components are fixed whenever an absolute estimate is possible and otherwise are allowed to float freely in fitting, as follows. (1) Wrong tag: fixed based on the MC-estimated ratio of the correctly reconstructed yields to the wrongly reconstructed yields. (We float this component in assessing associated systematic uncertainties.) (2) Wrong photon: ratio to the signal component is fixed according to the MC estimation. (3) Wrong track: fixed according to a MC estimation for which the MC sample is scaled to the N_{ST} observed in data. (4) τ decays to final states other than $\pi^+\bar{\nu}_\tau$: constrained to the signal yield, $D_s^+ \rightarrow \tau^+(\rightarrow \pi^+\bar{\nu}_\tau)\nu_\tau$. (5) Remainder: floated freely.

Normalizations of the two signal components ($D_s^+ \rightarrow \mu\nu_\mu$ and $\tau^+\nu_\tau$) are floated freely, except for the constraints introduced by the simultaneous fit and the ratio of the yields between the μ -like and π -like samples. This

ratio is fixed for each of the six datasets based on MC estimations.

The means of the convolved Gaussian functions in fitting $M_{inv}(D_s^-)$ and M_{miss}^2 are floated for both data and MC simulations. The widths are floated in fitting to data and are fixed to a negligibly small value in fitting to MC samples. Because the $M_{inv}(D_s^-)$ resolution depends on the D_s^- decay mode, the $M_{inv}(D_s^-)$ PDF is obtained as a sum of PDFs for all tag modes, weighted by the observed N_{ST} . We obtain the M_{miss}^2 PDFs in a similar way, as MC simulation predicts weak tag-mode dependence. The coefficients of the Chebyshev polynomials for backgrounds (1) and (5) are shared because MC simulations demonstrate that the statistical sensitivity of our data is insufficient to distinguish their slopes.

We determine $\epsilon_{DT}^{\ell\nu}$ for each of the thirteen tag modes by counting the reconstructed candidates that match the MC-generated true signal particles. The resultant efficiencies are shown in Tables III and IV.

To validate these DT efficiencies and our overall fitting procedure, we perform tests on ten independent data-size MC samples and compare the fitted signal yields and the corresponding branching fractions. Table V shows the differences between the fitted signal yields and the MC-predicted yields for the data-size samples and for a $40\times$ sample. We see reasonable agreement between the fitted and generated yields.

Figure 4 shows projections of the selected data sample onto the M_{miss}^2 and $M_{inv}(D_s^-)$ axes, summed over the six data samples. Scaled MC distributions are overlaid, with a breakdown of the components of the MC-simulated background. There is agreement between data and MC simulation for both signal and background. Figures 5 and 6 show comparisons between data and MC samples for signal-track momentum and the cosine of the polar angle, again demonstrating excellent agreement.

2. Fitting to data

The fitting procedure described in Sec. III B accounts for all signal and background processes that have been observed experimentally to date. We now introduce two additional physics processes that are expected theoretically but have not yet been observed, $D_s^+ \rightarrow \gamma\mu^+\nu_\mu$ and $D_s^+ \rightarrow \pi^+\pi^0$.

The radiative leptonic decay $D_s^+ \rightarrow \gamma\mu^+\nu_\mu$ is not helicity suppressed, but its experimental detection is difficult and has not yet been achieved. Past measurements of D_s^+ leptonic decays [20, 21] have relied on theoretical predictions of the branching fraction for this mode, with a 1% (relative) systematic uncertainty. For our analysis we note that the M_{miss}^2 distribution for $D_s^+ \rightarrow \gamma\mu^+\nu_\mu$ must have a high-side tail and could therefore affect our signal fits significantly. We generate a signal MC sample for this process following the procedure of previous BE-SIII studies of $D^+ \rightarrow \gamma e^+\nu_e$ [22] and $D_s^+ \rightarrow \gamma e^+\nu_e$ [23]. This adopts a factorization approach [24] in modeling

TABLE III. DT reconstruction efficiencies (in %) with statistical uncertainties for $D_s^+ \rightarrow \mu^+ \nu_\mu$ signal events in each of the thirteen tag modes. These efficiencies do not include the following intermediate-state branching fractions: $K_S^0 \rightarrow \pi^+ \pi^-$, $\pi^0 \rightarrow \gamma\gamma$, $\eta \rightarrow \gamma\gamma$, $\eta_{3\pi} \rightarrow \pi^+ \pi^- \pi^0$, $\eta'_{\pi\pi\eta} \rightarrow \pi^+ \pi^- \eta$, $\eta'_{\gamma\rho} \rightarrow \gamma\rho^0$, and $\rho \rightarrow \pi\pi$.

Tag mode	4180	4190	4200	4210	4220	4230
$K_S^0 K^-$	23.23 ± 0.12	23.06 ± 0.17	23.32 ± 0.18	22.33 ± 0.17	22.64 ± 0.18	23.80 ± 0.18
$K^- K^+ \pi^-$	19.84 ± 0.05	19.63 ± 0.07	19.63 ± 0.07	19.25 ± 0.07	19.52 ± 0.07	20.37 ± 0.07
$K_S^0 K^- \pi^0$	10.54 ± 0.09	10.29 ± 0.13	10.46 ± 0.13	10.43 ± 0.13	10.11 ± 0.13	10.80 ± 0.13
$K^- K^+ \pi^- \pi^0$	6.88 ± 0.03	6.78 ± 0.04	7.01 ± 0.04	6.89 ± 0.04	6.92 ± 0.05	7.36 ± 0.05
$K_S^0 K^- \pi^+ \pi^-$	11.14 ± 0.11	10.82 ± 0.16	11.24 ± 0.17	10.61 ± 0.16	10.94 ± 0.17	11.70 ± 0.17
$K_S^0 K^+ \pi^- \pi^-$	12.13 ± 0.09	11.88 ± 0.13	12.02 ± 0.13	11.78 ± 0.13	11.81 ± 0.13	12.72 ± 0.13
$\pi^- \pi^+ \pi^-$	26.88 ± 0.12	26.64 ± 0.17	26.56 ± 0.17	26.07 ± 0.17	26.12 ± 0.17	27.71 ± 0.18
$\pi^- \eta_{\gamma\gamma}$	25.24 ± 0.15	24.80 ± 0.22	24.87 ± 0.22	24.53 ± 0.22	24.48 ± 0.22	25.41 ± 0.22
$\rho^- \eta_{\gamma\gamma}$	12.54 ± 0.05	12.40 ± 0.07	12.32 ± 0.07	12.29 ± 0.07	12.25 ± 0.07	12.80 ± 0.08
$\rho^- \eta_{3\pi}$	5.35 ± 0.05	5.20 ± 0.07	5.29 ± 0.07	5.12 ± 0.07	5.05 ± 0.07	5.39 ± 0.07
$\pi^- \eta'_{\pi\pi\eta}$	13.48 ± 0.12	13.35 ± 0.18	13.19 ± 0.18	13.17 ± 0.18	13.33 ± 0.18	13.99 ± 0.18
$\pi^- \eta'_{\gamma\rho}$	19.43 ± 0.11	18.91 ± 0.16	19.02 ± 0.16	19.05 ± 0.16	18.84 ± 0.16	20.04 ± 0.16
$K^- \pi^+ \pi^-$	23.31 ± 0.16	22.72 ± 0.23	23.41 ± 0.23	22.57 ± 0.23	22.51 ± 0.23	23.82 ± 0.23

TABLE IV. DT reconstruction efficiencies (in %) with statistical uncertainties for $D_s^+ \rightarrow \tau^+ (\rightarrow \pi \bar{\nu}_\tau) \nu_\tau$ signal events in each of the thirteen tag modes. These efficiencies do not include the following intermediate-state branching fractions: $K_S^0 \rightarrow \pi^+ \pi^-$, $\pi^0 \rightarrow \gamma\gamma$, $\eta \rightarrow \gamma\gamma$, $\eta_{3\pi} \rightarrow \pi^+ \pi^- \pi^0$, $\eta'_{\pi\pi\eta} \rightarrow \pi^+ \pi^- \eta$, $\eta'_{\gamma\rho} \rightarrow \gamma\rho^0$, and $\rho \rightarrow \pi\pi$.

Tag mode	4180	4190	4200	4210	4220	4230
$K_S^0 K^-$	9.79 ± 0.08	9.66 ± 0.12	9.76 ± 0.12	9.32 ± 0.12	9.62 ± 0.12	9.83 ± 0.12
$K^- K^+ \pi^-$	8.33 ± 0.03	8.19 ± 0.05	8.30 ± 0.05	7.98 ± 0.05	8.03 ± 0.05	8.46 ± 0.05
$K_S^0 K^- \pi^0$	4.34 ± 0.06	4.28 ± 0.08	4.19 ± 0.08	4.16 ± 0.08	4.09 ± 0.08	4.35 ± 0.08
$K^- K^+ \pi^- \pi^0$	2.83 ± 0.02	2.78 ± 0.03	2.84 ± 0.03	2.79 ± 0.03	2.81 ± 0.03	2.92 ± 0.03
$K_S^0 K^- \pi^+ \pi^-$	4.60 ± 0.07	4.58 ± 0.11	4.54 ± 0.11	4.47 ± 0.11	4.55 ± 0.11	4.80 ± 0.11
$K_S^0 K^+ \pi^- \pi^-$	5.14 ± 0.06	4.87 ± 0.09	4.98 ± 0.09	4.83 ± 0.09	4.89 ± 0.09	5.17 ± 0.09
$\pi^- \pi^+ \pi^-$	11.26 ± 0.08	11.10 ± 0.12	11.11 ± 0.12	10.77 ± 0.12	10.96 ± 0.12	11.75 ± 0.13
$\pi^- \eta_{\gamma\gamma}$	10.44 ± 0.11	10.41 ± 0.16	10.19 ± 0.16	10.25 ± 0.16	10.21 ± 0.16	10.14 ± 0.16
$\rho^- \eta_{\gamma\gamma}$	5.05 ± 0.03	5.06 ± 0.05	4.96 ± 0.05	4.89 ± 0.05	4.91 ± 0.05	5.05 ± 0.05
$\rho^- \eta_{3\pi}$	2.11 ± 0.03	2.11 ± 0.04	2.01 ± 0.04	1.95 ± 0.04	2.04 ± 0.04	2.18 ± 0.04
$\pi^- \eta'_{\pi\pi\eta}$	5.64 ± 0.08	5.43 ± 0.12	5.45 ± 0.12	5.51 ± 0.12	5.39 ± 0.12	5.66 ± 0.12
$\pi^- \eta'_{\gamma\rho}$	8.16 ± 0.07	8.08 ± 0.11	8.09 ± 0.11	7.99 ± 0.11	7.94 ± 0.11	8.10 ± 0.11
$K^- \pi^+ \pi^-$	9.71 ± 0.11	9.41 ± 0.16	9.78 ± 0.16	9.77 ± 0.16	9.47 ± 0.16	9.78 ± 0.16

$D_s^+ \rightarrow \gamma \mu^+ \nu_\mu$ events, requiring a minimum photon energy of 10 MeV. Figure 7 shows the predicted M_{miss}^2 distribution for $D_s^+ \rightarrow \gamma \mu^+ \nu_\mu$, along with distributions for other processes. Because of the high-side tail of the distribution for $D_s^+ \rightarrow \gamma \mu^+ \nu_\mu$, we explicitly include this additional PDF in fitting our data.

We estimate the scale of the $D_s^+ \rightarrow \gamma \mu^+ \nu_\mu$ contribution based on theoretical predictions of the branching fraction. G. Burdman, J. T. Goldman, and D. Wyler [25] predict $\mathcal{B}(D_s^+ \rightarrow \gamma \mu^+ \nu_\mu) \sim 10^{-4}$ and $\mathcal{B}(D^+ \rightarrow \gamma \mu^+ \nu_\mu) \sim 10^{-5}$, while J. C. Yang and M. Z. Yang estimate $\mathcal{B}(D^+ \rightarrow \gamma \mu^+ \nu_\mu)$ to be 3.64×10^{-5} [26]. Comparing these to the measured branching fractions of nonradiative leptonic decays, $\mathcal{B}(D^+ \rightarrow \mu^+ \nu_\mu) = (3.74 \pm 0.17) \times 10^{-4}$ [1] and $\mathcal{B}(D_s^+ \rightarrow \mu^+ \nu_\mu) = (5.49 \pm 0.16) \times 10^{-3}$ [1], we adopt the ratio $R_\gamma = \mathcal{B}(D_{(s)}^+ \rightarrow \gamma \mu^+ \nu_\mu) / \mathcal{B}(D_{(s)}^+ \rightarrow \mu^+ \nu_\mu) = 0.1$ as a constraint in our fits. The estimated number of recon-

structed radiative events in our signal sample is about 1% of the nonradiative events, which is consistent with previous publications ([20, 21]). In assessing the systematic uncertainty associated with this assumption, we vary R_γ by ± 0.1 .

The suppressed hadronic decay $D_s^+ \rightarrow \pi^+ \pi^0$ has not been observed, with only an upper limit on the branching fraction of $\mathcal{B}(D_s^+ \rightarrow \pi^+ \pi^0) < 3.4 \times 10^{-4}$ at 90% confidence level [1]. Events of this type exhibit a clear peak in M_{miss}^2 , as is demonstrated by MC simulation and shown in Fig. 7. We do not include $D_s^+ \rightarrow \pi^+ \pi^0$ in our nominal data fit, but introduce it with a branching fraction equal to the upper limit as a systematic variation.

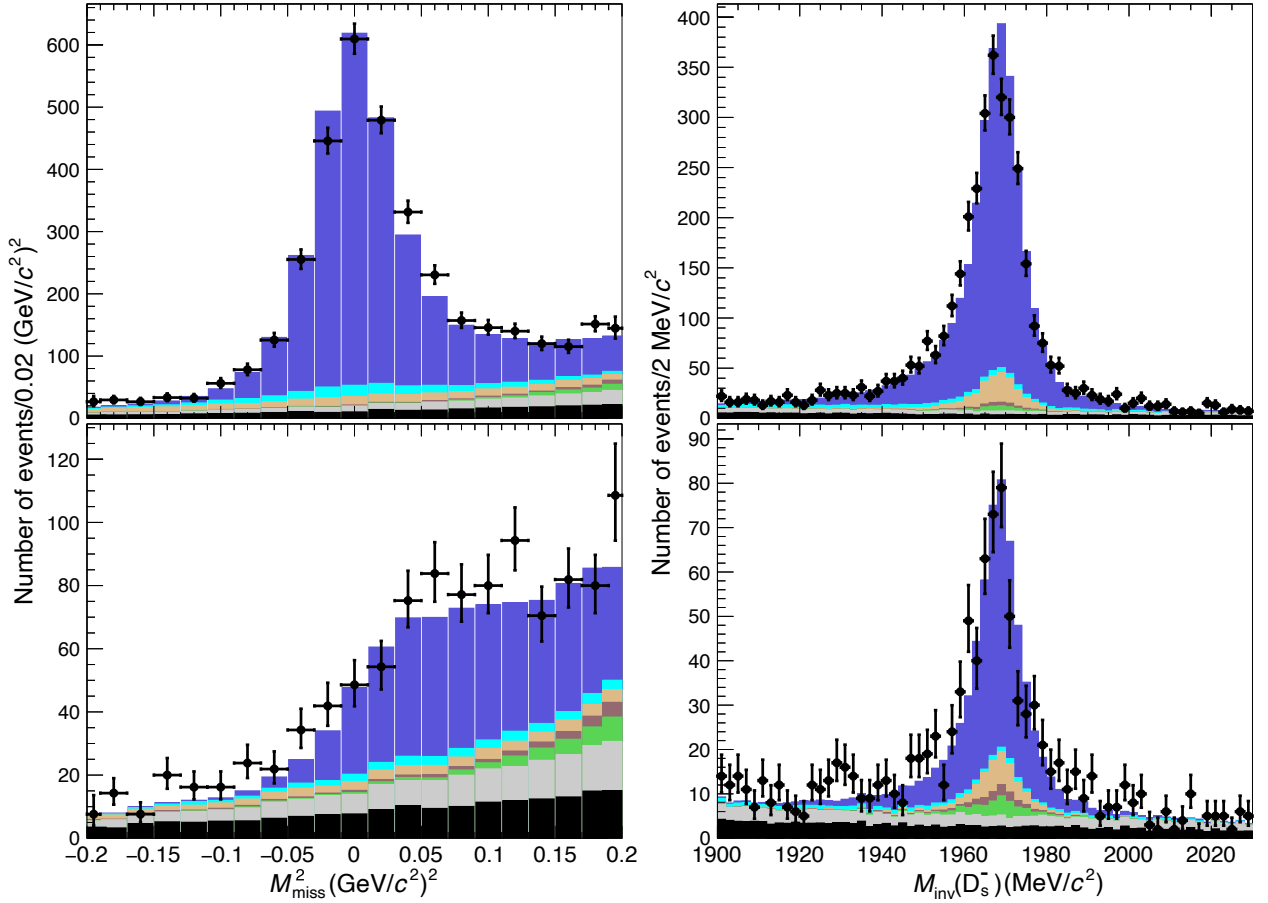


FIG. 4. Projections onto the M_{miss}^2 (left) and $M_{\text{inv}}(D_s^-)$ (right) axes, for μ -like (top) and π -like (bottom) candidates. Black points are data, summed over all six samples. The filled histograms represent the prediction of the $40\times$ MC sample, normalized to the integrated luminosity of data, with the $D_s^+ \rightarrow \mu^+\nu_\mu$ and $\tau^+(\rightarrow \pi^+\bar{\nu}_\tau)\nu_\tau$ signal on top (blue). Background components are stacked below this in the following order from the top to the bottom: tag-side misreconstructed (cyan), misreconstructed transition photon (light brown), signal side misreconstructed (dark brown), $D_s^+ \rightarrow \tau^+\nu_\tau$, where the τ^+ decays to a final state other than $\pi^+\bar{\nu}_\tau$ (green), other charm background (gray), and noncharm sources (black, at bottom).

3. Branching fraction results

Figure 8 shows our nominal fit to the 4180 data sample with scaled MC components overlaid. (Figures showing fit results for the other five datasets are provided as supplemental material [27].) The fit to all data samples yields 2198 ± 55 $D_s^+ \rightarrow \mu^+\nu_\mu$ events and 946_{-45}^{+46} $D_s^+ \rightarrow \tau^+(\rightarrow \pi^+\bar{\nu}_\tau)\nu_\tau$ events. The measured branching fractions and statistical uncertainties following from these event yields are $\mathcal{B}(D_s^+ \rightarrow \mu^+\nu_\mu) = (5.35 \pm 0.13) \times 10^{-3}$ and $\mathcal{B}(D_s^+ \rightarrow \tau^+\nu_\tau) = (5.21 \pm 0.25)\%$, where we assume $\mathcal{B}(\tau^+ \rightarrow \pi^+\bar{\nu}_\tau) = 10.82\%$ [1]. Our two measurements of the D_s^+ leptonic branching fractions have the best statistical precision to date.

We also report the ratio of the two branching fractions, $R = \Gamma(D_s^+ \rightarrow \tau^+\nu_\tau)/\Gamma(D_s^+ \rightarrow \mu^+\nu_\mu) = 9.73_{-0.58}^{+0.61}$, where the statistical uncertainty includes the observed anticorrelation between the two components.

An alternative procedure that provides a more statistically precise but model-dependent determination of

$\mathcal{B}(D_s^+ \rightarrow \tau^+\nu_\tau)$ is to fit our data with the ratio R fixed to the SM prediction of 9.75. This fit yields a $D_s^+ \rightarrow \tau^+(\rightarrow \pi^+\bar{\nu}_\tau)\nu_\tau$ signal of 946 ± 18 events and $\mathcal{B}(D_s^+ \rightarrow \tau^+\nu_\tau) = (5.22 \pm 0.10)\%$.

Because of this anticorrelation between the $D_s^+ \rightarrow \mu^+\nu_\mu$ and $D_s^+ \rightarrow \tau^+\nu_\tau$ signal processes, caution is necessary in extracting the decay constant $f_{D_s^+}$ and CKM matrix element $|V_{cs}|$ from an average of the measured branching fractions. We circumvent this difficulty by requiring lepton flavor universality (LFU), which requires that values of $f_{D_s^+}|V_{cs}|$ extracted from $\mathcal{B}(D_s^+ \rightarrow \mu^+\nu_\mu)$ and $\mathcal{B}(D_s^+ \rightarrow \tau^+\nu_\tau)$ be identical. From Eqs. (1) and (2), it can be seen that this LFU constraint is equivalent to the condition $R = 9.75$. Thus, in Sec. V we present our combined average value of $f_{D_s^+}|V_{cs}|$ by using the measurement obtained with the constraint $R = 9.75$.

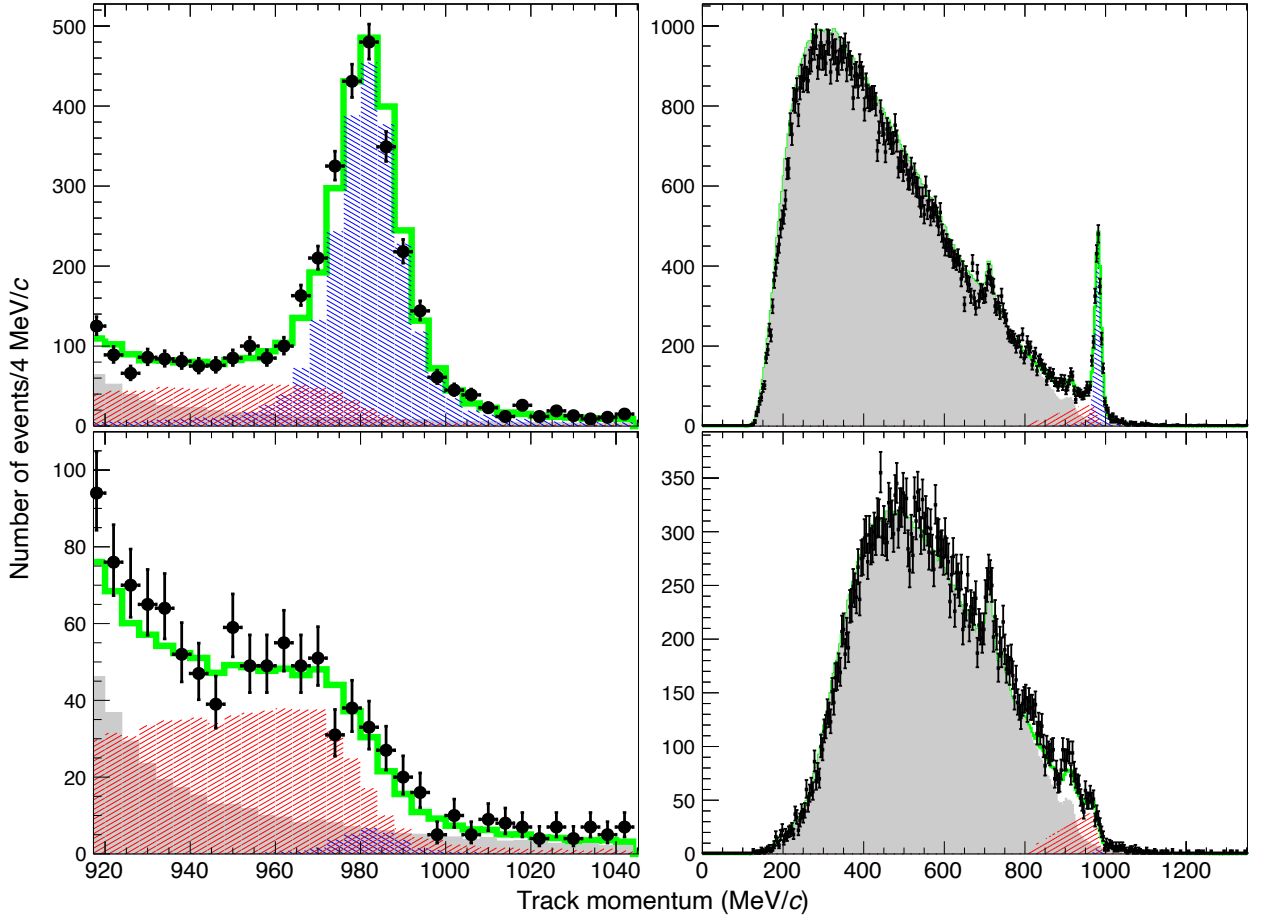


FIG. 5. Distributions of the momentum of signal candidate tracks in the D_s^+ rest frame for the DT sample with the additional requirement $1900 < M_{\text{inv}}(D_s^-) < 2030 \text{ MeV}/c^2$ for the μ -like (top) and the π -like samples (bottom). The black points are data and the overlaid histograms represent the $40\times$ MC sample (normalized to the integrated luminosity of data), with green for the total, gray filled for the total background, and crosshatched for the signals, $D_s^+ \rightarrow \mu^+\nu_\mu$ (blue, top-left to bottom-right) and $D_s^+ \rightarrow \tau^+(\rightarrow \pi^+\bar{\nu}_\tau)\nu_\tau$ (red, bottom-left to top-right). The distributions shown on the left correspond to only $-0.20 < M_{\text{miss}}^2 < 0.20 \text{ (GeV}/c^2)^2$, while we show the entire momentum spectra on the right.

4. CP -violating Asymmetries

We also measure the CP -violating asymmetries,

$$A_{CP} = \frac{\Gamma(D_s^+ \rightarrow \ell^+\nu_\ell) - \Gamma(D_s^- \rightarrow \ell^-\bar{\nu}_\ell)}{\Gamma(D_s^+ \rightarrow \ell^+\nu_\ell) + \Gamma(D_s^- \rightarrow \ell^-\bar{\nu}_\ell)}, \quad (5)$$

where $\ell = \mu$ or τ . Procedures are identical to those applied to the full sample, except that we determine the branching fractions separately for D_s^+ and D_s^- .

To search for systematic effects specific to this measurement, we look at $\Delta N_{\text{tag}}^\pm = \sum_i \frac{N_{\text{tag},i}^+ - N_{\text{tag},i}^-}{N_{\text{tag},i}^+ + N_{\text{tag},i}^-}$, where i runs over the thirteen tag modes and $N_{\text{tag},i}^\pm = N_{ST,i}^\pm / \epsilon_{ST,i}^\pm$ for $D_s^\pm \rightarrow i$ mode, and we combine the six datasets. We obtain $\Delta N_{\text{tag}}^\pm = (+0.6 \pm 0.8)\%$, consistent with zero CP asymmetry, which involves the simulations of charge-dependent tracking and PID efficiencies. We conservatively assign 1.0% (0.6% and 0.8% combined in quadrature) as a possible systematic uncertainty due

to charge dependence in particle reconstruction and assign no additional systematic uncertainty to our measurements. Potential systematic effects that are associated with our DT fitting procedure are canceled in the determination of A_{CP} .

The nominal fit yields 1123 ± 40 events and 463_{-32}^{+33} events for $D_s^- \rightarrow \mu^-\nu_\mu$ and $D_s^- \rightarrow \tau^-\nu_\tau$ candidates, respectively, and 1077 ± 38 events and 487_{-32}^{+33} events for $D_s^+ \rightarrow \mu^+\nu_\mu$ and $D_s^+ \rightarrow \tau^+\nu_\tau$ candidates, respectively. Table VI shows the resultant branching fractions for D_s^+ and D_s^- , as well as A_{CP} , based on the two fitting methods: our principal method, which yields both $\mathcal{B}(D_s^+ \rightarrow \mu^+\nu_\mu) (\equiv \mathcal{B}_{\mu\nu})$ and $\mathcal{B}(D_s^+ \rightarrow \tau^+\nu_\tau) (\equiv \mathcal{B}_{\tau\nu})$, and the alternative method imposing the SM constraint, labeled as $\mathcal{B}_{\tau\nu}^{\text{SM}}$. The first uncertainties quoted in A_{CP} are statistical and the second systematic. All three A_{CP} values show no evidence of CP violation. This is the first measurement of $A_{CP}(\tau\nu)$ and the most precise determinations to date of both $A_{CP}(\mu\nu)$ and $A_{CP}(\tau\nu)^{\text{SM}}$.

TABLE V. Relative difference in % between the measured signal yields and generated numbers for ten “sets” of data-sized MC samples, the average of these, and a $40\times$ MC sample.

Set	Relative Difference of $\mu\nu$ Yield	Relative Difference of $\tau\nu$ Yield
01	$+0.41 \pm 2.43$	-1.54 ± 4.27
02	-0.76 ± 2.39	$+2.09 \pm 4.07$
03	$+1.09 \pm 2.43$	$+1.96 \pm 4.25$
04	-1.21 ± 2.45	$+3.10 \pm 4.20$
05	$+0.40 \pm 2.37$	-0.87 ± 4.37
06	-0.09 ± 2.38	$+3.32 \pm 4.10$
07	-2.85 ± 2.41	$+3.61 \pm 5.01$
08	$+1.12 \pm 2.40$	$+0.25 \pm 4.21$
09	$+0.29 \pm 2.34$	-1.91 ± 4.45
10	-1.18 ± 2.37	-3.27 ± 4.26
Average	-0.52 ± 0.76	$+0.57 \pm 1.36$
$40\times$	-0.30 ± 0.39	-0.68 ± 0.70

TABLE VI. Summary of charge-dependent branching fractions and A_{CP} (in %) for $\mathcal{B}(D_s^+ \rightarrow \mu^+\nu_\mu)$ and $\mathcal{B}(D_s^+ \rightarrow \tau^+\nu_\tau)$. The uncertainties reported in branching fractions are only statistical. The first uncertainties quoted in A_{CP} are statistical and the second systematic.

	D_s^-	D_s^+	Combined
$\mathcal{B}_{\mu\nu} \times 10^3$	5.40 ± 0.19	5.28 ± 0.19	5.35 ± 0.13
$\mathcal{B}_{\tau\nu} \times 10^2$	$5.07^{+0.36}_{-0.35}$	$5.37^{+0.36}_{-0.35}$	5.21 ± 0.25
$\mathcal{B}_{\tau\nu}^{\text{SM}} \times 10^2$	5.21 ± 0.14	5.20 ± 0.14	5.22 ± 0.10
$A_{CP}(\mu^\pm\nu)$		$-1.2 \pm 2.5 \pm 1.0$	
$A_{CP}(\tau^\pm\nu)$		$+2.9 \pm 4.8 \pm 1.0$	
$A_{CP}(\tau^\pm\nu)^{\text{SM}}$		$-0.1 \pm 1.9 \pm 1.0$	

IV. SYSTEMATIC UNCERTAINTIES

We consider a wide variety of potential sources of systematic uncertainty in our measurements of the branching fractions $\mathcal{B}(D_s^+ \rightarrow \mu^+\nu_\mu)$ and $\mathcal{B}(D_s^+ \rightarrow \tau^+\nu_\tau)$, and their ratio R . Procedures are described in the following two subsections and the resulting estimates are listed in Table VII. The sources of systematic uncertainty subdivide into two categories. Sources associated with the two-dimensional simultaneous DT fitting procedure affect all measurements, while those that are not related to fitting largely cancel in measuring the ratio R .

A. Nonfitting systematic uncertainties

We directly estimate the systematic uncertainties associated with the two input branching fractions, $\mathcal{B}(D_s^* \rightarrow \gamma D_s)$ and $\mathcal{B}(\tau^+ \rightarrow \pi^+\bar{\nu}_\tau)$, by propagating the uncertain-

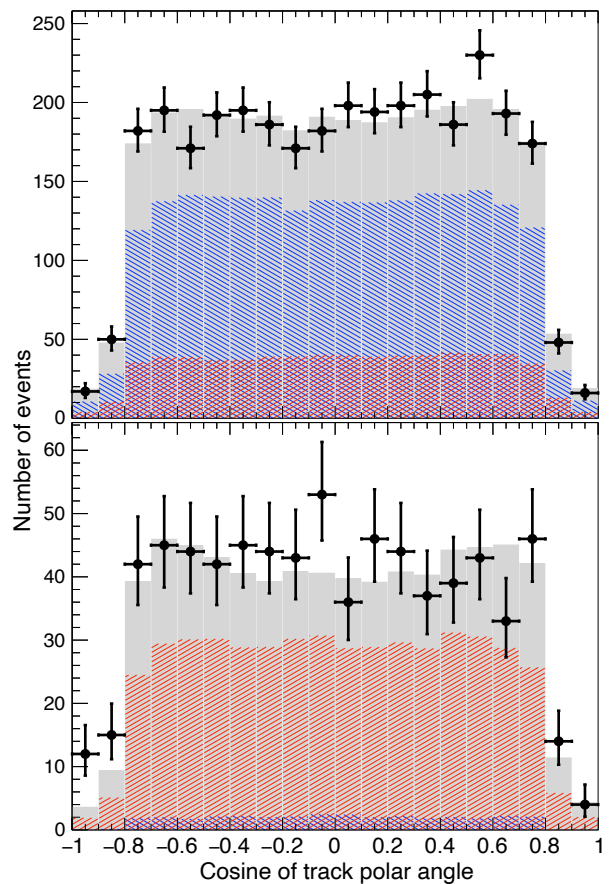


FIG. 6. Distributions of cosines of polar angles in the D_s^+ rest frame of μ -like (top) and π -like (bottom) signal-candidate tracks, based on the nominal DT selection and the additional requirements $1930 < M_{\text{inv}}(D_s^-) < 1990 \text{ MeV}/c^2$ and $-0.1 < M_{\text{miss}}^2 < +0.2 (\text{GeV}/c^2)^2$. Black points are data and the overlaid histograms correspond to the $40\times$ MC sample scaled to the integrated luminosity of data, with gray shading for the total, and crosshatched for the signals, $D_s^+ \rightarrow \mu^+\nu_\mu$ (blue, top-left to bottom-right) and $D_s^+ \rightarrow \tau^+(\rightarrow \pi^+\bar{\nu}_\tau)\nu_\tau$ (red, bottom-left to top-right), respectively. The difference between gray and (the sum of red and blue) is the background.

ties from Ref. [1].

We estimate the systematic uncertainty associated with the reconstruction of the signal track, μ or π , by reconstructing events from the continuum process $e^+e^- \rightarrow K^+K^-\pi^+\pi^-$. By comparing the pion reconstruction efficiency over the relevant momentum range for 4180 data and MC samples, the reliability of the simulation is found to be better than 1%. The stability of tracking over our six data samples is demonstrated by consistent performance on control samples of radiative μ -pair events. On this basis we assign a 1% systematic uncertainty for our branching fraction measurements.

The systematic uncertainty associated with the reconstruction of the photon from $D_s^* \rightarrow \gamma D_s$ is estimated by reconstructing $J/\psi \rightarrow \pi^+\pi^-\pi^0$ events [28]. Comparison of the photon-reconstruction efficiency in data and MC

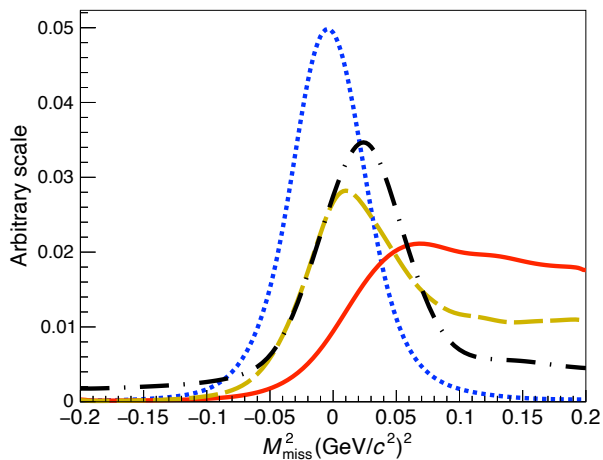


FIG. 7. Comparison of M_{miss}^2 distributions for various types of MC events for the μ -like case. (Shapes are very similar for the π -like case.) The dotted-blue line represents $D_s^+ \rightarrow \mu^+ \nu_\mu$, solid-red is $D_s^+ \rightarrow \tau^+ (\rightarrow \pi^+ \bar{\nu}_\tau) \nu_\tau$, dashed-orange is $D_s^+ \rightarrow \gamma \mu^+ \nu_\mu$, and dotted-dashed-black is $D_s^+ \rightarrow \pi^+ \pi^0$. All distributions are normalized to unity.

samples gives a 1% systematic uncertainty for this source.

In selecting our signal-side sample, we require that there be only one charged track in addition to the daughters of the reconstructed tag, as described in Sec. III B. We estimate the systematic uncertainty for this requirement based on double-hadronic-tag (DHT) events in which a D_s^- is tagged in one of our thirteen modes, while the D_s^+ decays into either $K_S^0 \pi$ or $KK\pi$. The uncertainty is 0.2% for all three branching fraction measurements.

As described in Sec. III A, we handle events with multiple ST candidates for a given D_s mode and charge by choosing the one with E_γ , the $D_s^* \rightarrow \gamma D_s$ photon energy in the D_s^* rest frame, closest to the expected value. We investigate systematic effects in this selection by comparing efficiencies for DHT events in data and MC samples. The agreement is found to have some dependence on event complexity (charged and neutral particle multiplicity), but is no worse than 1%, so we assign this as the systematic uncertainty in the best-photon selection for all branching fraction measurements.

Our signal-selection procedure (Sec. III B) includes three additional requirements that are designed to suppress events with unreconstructed particles. We study systematic uncertainties associated with these using the same DHT events. For the requirement $E_{\text{neu}}^{\text{max}} < 300$ MeV, we compare the efficiencies in data and MC samples for the standard requirement and probe the stability of the data/MC agreement by also testing with requirements less or more restrictive than this by 50 MeV. We find an uncertainty of 0.3% for all branching fractions. We similarly probe the $ANG > 40^\circ$ and $|\cos \theta_{\text{miss}}| < 0.90$ efficiencies, although in this case the results with the D_s DHT sample are limited by sample size. We augment with data collected at $E_{\text{cm}} = 3773$ MeV, with an integrated luminosity of 2.93 fb^{-1} , and copious

production of $\psi(3770) \rightarrow D\bar{D}$. In this sample we measure data and MC efficiencies for D^0 decays into the three hadronic modes, $K^- \pi^+$, $K^- \pi^+ \pi^0$, and $K^- \pi^+ \pi^- \pi^+$, and for the semileptonic decay $\bar{D}^0 \rightarrow K^+ e^- \bar{\nu}_e$. Based on these studies, we assign a 1% systematic uncertainty for the ANG and $|\cos \theta_{\text{miss}}|$ requirements for all branching fraction measurements.

The determination of the D_s leptonic branching fractions with Eqs. (3) and (4) depends on the efficiency ratios $\epsilon_{DT}^{\ell\nu,i}/\epsilon_{ST}^i$. Both ST and DT selection involve reconstructing a hadronic D_s^- decay, and we expect the efficiency for this tag reconstruction to depend on the event environment. The different topologies of leptonic D_s^+ decays (only one track) and generic D_s^+ decays (most with multiple tracks and showers) produce a mode-dependent bias in reconstructing the D_s^- tag that may be imperfectly modeled in the MC simulation. We estimate the systematic uncertainty associated with this effect by studying the BESIII detector's tracking and PID efficiencies for events with different particle multiplicities using the large $E_{\text{cm}} = 3773$ MeV data sample mentioned earlier. The size of this uncertainty varies among the three branching fraction and R measurements, as is shown in Table VII.

B. Fitting systematic uncertainties

To assess the systematic uncertainties associated with our fitting procedure, we generate toy Monte Carlo samples based on the observed data distributions. We fit to these toy samples while varying an analysis selection requirement (or fitting procedure, PID requirement, etc.) and take the difference between the averages of these ensembles with the nominal fit procedure and with the alternative procedure and assign it as a systematic uncertainty. Table VII shows that these estimated systematic uncertainties vary significantly among the measurements of the three branching fraction and R .

The uncertainty in the determination of the denominators in Eqs. (3) and (4) arises mainly from fitting to $M_{\text{inv}}(D_s^-)$ for ST candidates. The dominant effect comes from background and signal shapes (including the convolved Gaussian functions, which are independently determined for 4180, 4190–4220 and 4230). We also investigate the contamination from $e^+e^- \rightarrow \gamma_{ISR} D_s^+ D_s^-$, and find the uncertainty associated with this to be negligible.

For a conservative estimate of the uncertainty due to the assumption of a fixed ratio $R_\gamma = \mathcal{B}(D_{(s)}^+ \rightarrow \gamma \mu^+ \nu_\mu) / \mathcal{B}(D_{(s)}^+ \rightarrow \mu^+ \nu_\mu) = 0.1$, we vary R_γ by ± 0.1 .

To allow for the possible effect of the unobserved mode $D_s^+ \rightarrow \pi^+ \pi^0$, which is excluded from our nominal fit, we include the PDF for this mode in an alternative fit, with the normalization set to the experimental upper limit, $\mathcal{B}(D_s^+ \rightarrow \pi^+ \pi^0) < 3.4 \times 10^{-4}$.

We consider a possible systematic uncertainty due to π -ID efficiency, measuring the effect with the D_s and D^0

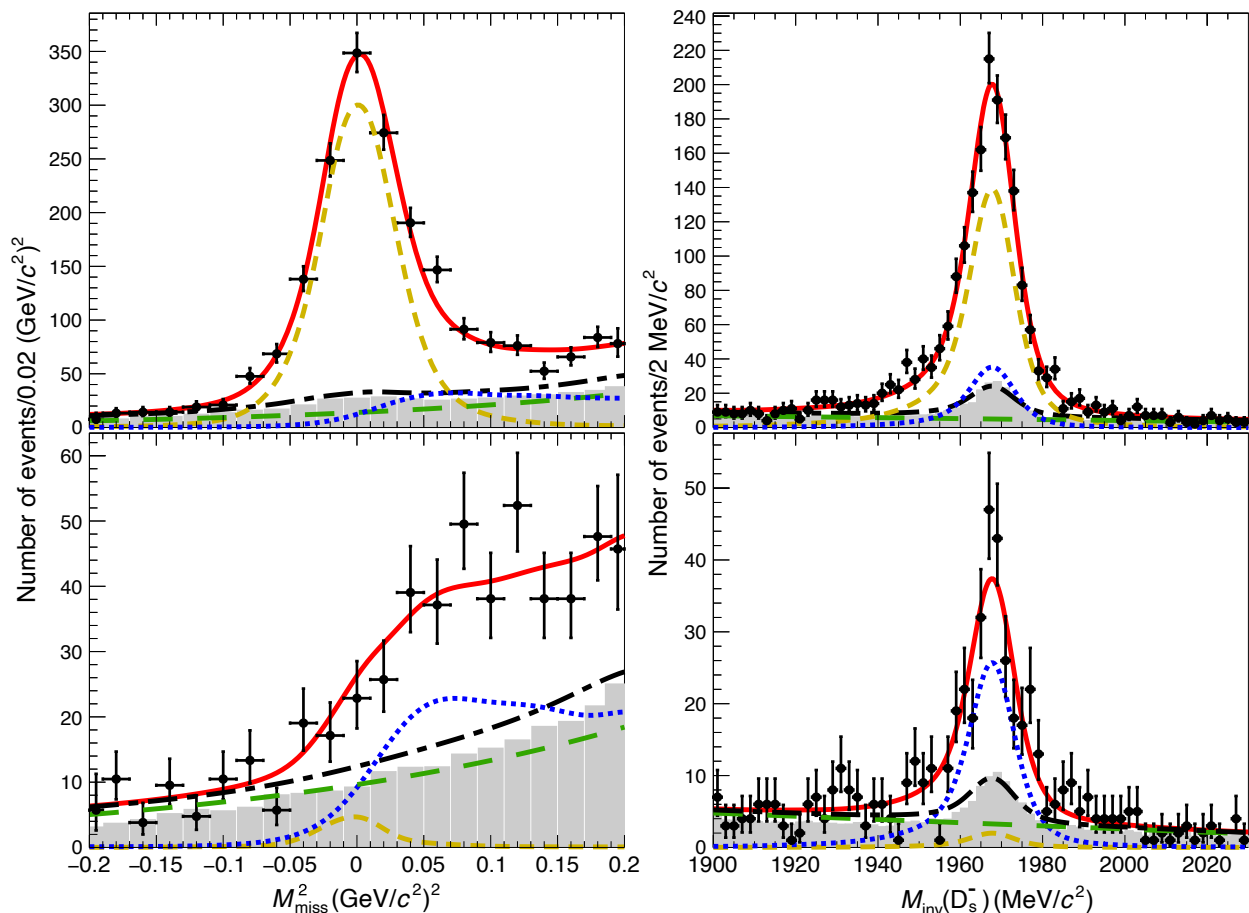


FIG. 8. Projections onto the M_{miss}^2 (left) and $M_{\text{inv}}(D_s^-)$ (right) axes of the two-dimensional fit to 4180 data for the μ -like (top) and the π -like (bottom) samples. Figures showing fit results for the other five datasets are provided as supplemental material [27]. The black points are data, the shaded histograms correspond to the $40\times$ background MC sample scaled to the integrated luminosity of data, and the lines represent the fitted signal and background shapes. The red-solid, orange-dashed, and blue-dotted lines represent the total, $D_s^+ \rightarrow \mu^+ \nu_\mu$, and $D_s^+ \rightarrow \tau^+ \nu_\tau$, while black-dot-dashed and green-long-dashed lines correspond to the total background and the case when both tag and signal sides are misreconstructed, respectively.

data samples mentioned in Sec. III B. The uncertainty due to the rate for misidentification of μ as π is estimated by comparing the rate between data and our MC simulation in the $D_s^+ \rightarrow \mu^+ \nu_\mu$ events, in which we heavily suppress the contribution from $D_s^+ \rightarrow \tau^+ (\tau^+ \rightarrow \pi^+ \bar{\nu}_\tau) \nu_\tau$ by requiring the signal track to penetrate deep into our MUC, as is done in Ref. [6].

In the nominal fitting procedure, we share two convolved Gaussian functions [one each for M_{miss}^2 and $M_{\text{inv}}(D_s^-)$] over the six data samples, effectively assuming that any data/MC differences are independent of E_{cm} and changes in running conditions. We estimate a possible uncertainty due to this assumption with an alternative fit using independent Gaussian functions for each of the 4180, 4190 – 4220 and 4230 data groups.

The relative size of the background component arising from misreconstruction on the tag side is fixed according to MC simulation in our nominal fit procedure. We estimate the potential systematic uncertainty introduced by this constraint with an alternative fit allowing this

component to float freely.

The relative size of the wrong-photon background component is also fixed in our nominal fitting procedure. For a systematic test, we vary this by $\pm 1.4\%$ (relative), the quadrature sum of a 1.0% uncertainty for photon reconstruction and a second 1.0% uncertainty for the best-photon selection method.

The size of the background component in which the signal track is misreconstructed is fixed in our nominal procedure to MC simulation, normalized to the ST yields in data. The primary source is the decay $D_s^+ \rightarrow K^0 \pi^+$, and we use the uncertainties in $\mathcal{B}(D_s^+ \rightarrow K_S^0 \pi^+)$ [1] and in our N_{ST} determination to estimate the systematic uncertainty in the estimate of this background component.

Background events in which both the tag side and the signal track are misreconstructed are parametrized in the nominal fit with a first-order Chebyshev polynomial for $M_{\text{inv}}(D_s^-)$ and a first-order exponential polynomial for M_{miss}^2 . We use a MC-based shape for $M_{\text{inv}}(D_s^-)$ and a

first-order Chebyshev polynomial for M_{miss}^2 in an alternative fit to estimate a possible systematic uncertainty due to the assumed background shape.

MC studies show that $D_s^+ \rightarrow \tau^+ \nu_\tau$ events with τ^+ decays into final states other than $\pi^+ \bar{\nu}_\tau$ that are counted as signal are dominated by $\tau^+ \rightarrow \mu^+ \nu_\mu \bar{\nu}_\tau$ and $\tau^+ \rightarrow \pi^+ \pi^0 \bar{\nu}_\tau$ for the μ -like sample and by $\tau^+ \rightarrow \pi^+ \pi^0 \bar{\nu}_\tau$ and $\tau^+ \rightarrow e^+ \nu_e \bar{\nu}_\tau$ for the π -like sample. We estimate the uncertainty in the estimate of these events with variations based on the uncertainties in the measured branching fractions [1].

In our nominal fitting procedure, we fix the relative yields of signal between the μ -like and π -like samples according to MC simulation. The μ -like and π -like samples are defined by $E_{\text{EMC}} \leq 300$ MeV and $E_{\text{EMC}} > 300$ MeV, respectively. Thus, to assess the systematic uncertainty associated with this criterion, we look at distributions of E_{EMC} and see how well our MC agrees with data. We look at distributions for muons from $D_s^+ \rightarrow \mu^+ \nu_\mu$ and for pions from $D^{*+} D^-$ and $D^{*+} D^{*-}$, with $D^{*+} \rightarrow D^0 \pi^+$ and $D^0 \rightarrow K^- \pi^+$, where the π^+ coming from the D^0 decay deposits E_{EMC} , while requiring $800 < |\vec{p}_\pi| < 1100$ MeV/ c to match our signal pion and muon tracks. We observe a 4% (relative) difference in partitioning rates between data and MC samples. We vary the rate by $\pm 4\%$ to estimate this systematic uncertainty.

As an alternative fitting procedure, we constrain the yields of $D_s^+ \rightarrow \mu^+ \nu_\mu$ and $D_s^+ \rightarrow \tau^+ \nu_\tau$ to the SM expectation for the ratio $R = 9.75$, derived from Eq. (2). The uncertainty in this prediction arises from the input particle masses, which are precisely known. We estimate a possible systematic uncertainty due to this constraint by varying R by ± 0.01 .

V. SUMMARY AND COMPARISONS TO OTHER EXPERIMENTAL RESULTS

Our measurements are summarized in Table VIII, along with previously published experimental results. In this section, the first uncertainty quoted is statistical and the second is systematic. We measure the absolute branching fraction $\mathcal{B}(D_s^+ \rightarrow \tau^+ \nu_\tau) = (5.21 \pm 0.25 \pm 0.17)\%$, which is the most precise measurement to date and is in agreement with the SM prediction of $\mathcal{B}(D_s^+ \rightarrow \tau^+ \nu_\tau) = (5.221 \pm 0.018)\%$ (see Sec. I for the predicted branching fractions). For the ratio of the two decay widths, we obtain $R = \Gamma(D_s^+ \rightarrow \tau^+ \nu_\tau) / \Gamma(D_s^+ \rightarrow \mu^+ \nu_\mu) = 9.73_{-0.58}^{+0.61} \pm 0.36$, which is also consistent with the SM prediction of 9.75. The precision of these measurements is limited by the sample size.

By constraining the ratio of the yields of $D_s^+ \rightarrow \mu^+ \nu_\mu$ and $D_s^+ \rightarrow \tau^+ \nu_\tau$ to the SM expectation $R = 9.75$, we gain statistical sensitivity and obtain $\mathcal{B}(D_s^+ \rightarrow \tau^+ \nu_\tau) = (5.22 \pm 0.10 \pm 0.14)\%$, which is limited by its systematic uncertainty.

We also obtain $\mathcal{B}(D_s^+ \rightarrow \mu^+ \nu_\mu) = (5.35 \pm 0.13 \pm 0.16) \times 10^{-3}$, which is again the most precise to date. It is con-

TABLE VII. Systematic uncertainties on $\mathcal{B}_{\mu\nu}$, $\mathcal{B}_{\tau\nu}$, $\mathcal{B}_{\tau\nu}^{\text{SM}}$, and R . The notation ‘‘cncl.’’ indicates that a systematic uncertainty cancels in the calculation of the branching fraction ratio R , and ‘‘neg.’’ signifies that an uncertainty is negligible.

Rel. Syst. Uncertainty (%)	$\mathcal{B}_{\mu\nu}$	$\mathcal{B}_{\tau\nu}$	$\mathcal{B}_{\tau\nu}^{\text{SM}}$	R
$\Delta\mathcal{B}(D_s^+ \rightarrow \gamma D_s)$	0.7	0.7	0.7	cncl.
$\Delta\mathcal{B}(\tau^+ \rightarrow \pi^+ \bar{\nu}_\tau)$...	0.5	0.5	0.5
μ or π tracking	1.0	1.0	1.0	cncl.
Photon reconstruction	1.0	1.0	1.0	cncl.
$N_{tk} = 1$	0.2	0.2	0.2	cncl.
$E_{\text{neu}}^{\text{max}} < 300$ MeV	0.3	0.3	0.3	cncl.
Best photon selection	1.0	1.0	1.0	cncl.
ANG and $ \cos \theta_{\text{miss}} $	1.0	1.0	1.0	cncl.
Tag bias	0.4	0.3	0.4	0.1
N_{ST} based norm.	0.8	0.8	0.8	0.1
$\Delta\Gamma(D_s^+ \rightarrow \gamma \mu^+ \nu_\mu)$	0.6	1.0	0.7	0.4
$\Delta\mathcal{B}(D_s^+ \rightarrow \pi^+ \pi^0)$	0.1	0.3	0.1	0.2
π -ID	0.6	0.5	0.6	1.1
Signal shape	0.2	0.5	0.2	0.6
Wrong tag	1.1	1.4	0.3	2.4
Wrong photon	0.1	0.2	0.1	0.1
Wrong μ or π	neg.	0.2	0.1	0.2
Wrong both tag and trk	1.0	0.8	0.6	1.8
Other τ decays	neg.	neg.	neg.	neg.
μ/π -like separation	0.3	0.6	0.6	1.5
ΔR	0.1	...
Total syst. uncertainty	2.9	3.2	2.7	3.7

sistent with the previously published BESIII result of $(5.49 \pm 0.16 \pm 0.15) \times 10^{-3}$ [6], which only analyzed the 4180 data, and supersedes that result. Note that the analysis methods and background compositions for these two BESIII analyses are very different. In Ref. [6], we require μ identification with the MUC subdetector to suppress π from $D_s^+ \rightarrow \tau^+ \nu_\tau$, resulting in a smaller systematic uncertainty.

We also measure the CP -violating asymmetries $A_{CP}(\mu^\pm \nu) = (-1.2 \pm 2.5 \pm 1.0)\%$ and $A_{CP}(\tau^\pm \nu) = (+2.9 \pm 4.8 \pm 1.0)\%$. The former is the most precise to date and the latter is a first measurement. With the SM constraint, we have $A_{CP}(\tau^\pm \nu) = (-0.1 \pm 1.0 \pm 1.0)\%$, which is also the most precise to date. All three A_{CP} results show no evidence of CP violation.

The measured $\mathcal{B}(D_s^+ \rightarrow \tau^+ \nu_\tau)$ with the SM constraint leads to

$$f_{D_s^+} |V_{cs}| = (243.2 \pm 2.3 \pm 3.3 \pm 1.0) \text{ MeV},$$

where the last uncertainty comes from the external inputs (lepton masses, m_{D_s} , and the D_s^+ lifetime [1]). Table VIII presents results based on other fitting schemes. By taking $|V_{cs}| = 0.97320 \pm 0.00011$ from the constrained global fit [1] and the average of the recent four-flavor LQCD predictions, $f_{D_s^+} = (249.9 \pm 0.5) \text{ MeV}$ [3], one finds an expected product of these of $(243.2 \pm 0.5) \text{ MeV}$, in excellent agreement with our result.

By taking $|V_{cs}| = 0.97320 \pm 0.00011$ [1] as an input, we

obtain

$$f_{D_s^+} = 249.8 \pm 3.0 \pm 3.7 \pm 1.0 \text{ MeV}, \\ 249.7 \pm 6.0 \pm 4.1 \pm 1.0 \text{ MeV}, \text{ and} \\ 249.9 \pm 2.4 \pm 3.4 \pm 1.0 \text{ MeV},$$

from $\mathcal{B}_{\mu\nu}$, $\mathcal{B}_{\tau\nu}$, and $\mathcal{B}_{\tau\nu}$ with the SM constraint, respectively. All of these are in excellent agreement with the LQCD predictions. Similarly, by taking $f_{D_s^+} = 249.9 \pm 0.5 \text{ MeV}$ [3] as an input, we arrive at

$$|V_{cs}| = 0.973 \pm 0.012 \pm 0.015 \pm 0.004, \\ 0.972 \pm 0.023 \pm 0.016 \pm 0.004, \text{ and} \\ 0.973 \pm 0.009 \pm 0.013 \pm 0.004,$$

based on $\mathcal{B}_{\mu\nu}$, $\mathcal{B}_{\tau\nu}$, and $\mathcal{B}_{\tau\nu}$ with the SM constraint, respectively. Again they are in agreement with the global fit result [1].

Note that in the extraction of $f_{D_s^+}$ and comparison to the global fit result above, we treat as negligible the correlation arising from the overlap of $\sim 50\%$ of our data sample with that of Ref. [6], which is incorporated in the global fit result [1].

Table VIII also shows averages of $f_{D_s^+}|V_{cs}|$ for the current work and previous measurements. We combine the results from the two modes, $\mu^+\nu$ and $\tau^+\nu$, under the assumption of the LFU, employing those measurements with the constraint $R = 9.75$ to obtain the combined average value. As the analysis technique utilized in Refs. [29, 31] is essentially identical to this work, we also employ their measurements with the SM constraint for the calculation of the combined average.

We can also use our D_s^+ and previous D^+ results to compute $f_{D_s^+}/f_{D^+}$. LQCD predicts this with great precision, specifically $f_{D_s^+}/f_{D^+} = 1.1783 \pm 0.0016$ in Ref. [3]. From $\mathcal{B}(D^+ \rightarrow \mu^+\nu_\mu) = (3.74 \pm 0.17) \times 10^{-4}$ [1], $\tau_{D^+} = 1.040(7) \text{ ps}$ [1], and $|V_{cd}| = 0.22636 \pm 0.00048$ [1], we have $f_{D^+} = 202.9 \pm 4.7 \text{ MeV}$. Combining this with the $f_{D_s^+}$ we obtain with the SM constraint, we find $f_{D_s^+}/f_{D^+} = 1.232 \pm 0.035$, consistent with the LQCD

prediction within 1.5σ . The uncertainty on this ratio is now driven by the statistical uncertainty on the measurement of $\mathcal{B}(D^+ \rightarrow \mu^+\nu_\mu)$.

ACKNOWLEDGMENTS

The BESIII Collaboration thanks the staff of BEPCII and the computing center for their hard efforts. This work is supported in part by National Key Research and Development Program of China under Contracts Nos. 2020YFA0406400, 2020YFA0406300; National Natural Science Foundation of China (NSFC) under Contracts Nos. 11625523, 11635010, 11735014, 11822506, 11835012, 11935015, 11935016, 11935018, 11961141012; the Chinese Academy of Sciences (CAS) Large-Scale Scientific Facility Program; Joint Large-Scale Scientific Facility Funds of the NSFC and CAS under Contracts Nos. U1732263, U1832207; CAS Key Research Program of Frontier Sciences under Contracts Nos. QYZDJ-SSW-SLH003, QYZDJ-SSW-SLH040; 100 Talents Program of CAS; INPAC and Shanghai Key Laboratory for Particle Physics and Cosmology; ERC under Contract No. 758462; European Union Horizon 2020 research and innovation programme under Contract No. Marie Skłodowska-Curie grant agreement No 894790; German Research Foundation DFG under Contracts Nos. 443159800, Collaborative Research Center CRC 1044, FOR 2359, FOR 2359, GRK 214; Istituto Nazionale di Fisica Nucleare, Italy; Ministry of Development of Turkey under Contract No. DPT2006K-120470; National Science and Technology fund; Olle Engkvist Foundation under Contract No. 200-0605; STFC (United Kingdom); The Knut and Alice Wallenberg Foundation (Sweden) under Contract No. 2016.0157; The Royal Society, UK under Contracts Nos. DH140054, DH160214; The Swedish Research Council; U. S. Department of Energy under Contracts Nos. DE-FG02-05ER41374, DE-SC-0012069.

-
- [1] P.A. Zyla *et al.* (Particle Data Group), *Prog. Theor. Exp. Phys.* **2020**, 083C01 (2020).
- [2] R. Aaij *et al.* (LHCb Collaboration), *Phys. Rev. Lett.* **119**, 101801 (2017).
- [3] A. Aoki *et al.* (Flavour Lattice Averaging Group), *Eur. Phys. J. C* **80**, 113 (2020).
- [4] M. Ablikim *et al.* (BESIII Collaboration), *Nucl. Instrum. Methods Phys. Res., Sec. A* **614**, 345 (2010); *Chin. Phys. C* **44**, 040001 (2020).
- [5] C. H. Yu *et al.*, in *Proceedings of IPAC 2016, Busan, Korea, 2016*, ISBN 978-3-95450-147-2.
- [6] M. Ablikim *et al.* (BESIII Collaboration), *Phys. Rev. Lett.* **122**, 071802 (2019).
- [7] X. Li *et al.*, *Radiat. Detect. Technol. Methods* **1**, 13 (2017); Y. X. Guo *et al.*, *Radiat. Detect. Technol. Methods* **1**, 15 (2017).
- [8] The E_{cm} measurement is described in M. Ablikim *et al.* (BESIII Collaboration), *Chin. Phys. C* **40**, 063001 (2016), which includes the result for the 4230 data sample. E_{cm} values for the other data samples have been obtained by a similar procedure.
- [9] The integrated luminosity measurement is described in M. Ablikim *et al.* (BESIII Collaboration), *Chin. Phys. C* **39**, 093001 (2015), which includes the result for the 4230 data sample. The integrated luminosity values for the other data samples have been obtained by a similar procedure.
- [10] S. Agostinelli *et al.* (GEANT4 Collaboration), *Nucl. Instrum. Methods Phys. Res., Sec. A* **506**, 250 (2003); J. Allison *et al.*, *IEEE Trans. Nucl. Sci.* **53**, 270 (2006); Z. Y. Deng *et al.*, *Chin. Phys. C* **30**, 371 (2006) (in Chinese).

TABLE VIII. Our measured branching fractions and their corresponding products of the decay constant $f_{D_s^+}$ and the CKM matrix-element magnitude $|V_{cs}|$. The reconstructed τ -decay mode for each measurement is indicated in parentheses. Other experimental results are also shown for comparison. The entry labeled “BESIII @ 4180” is the BESIII result from Ref. [6], based only on the 4180 data sample and requiring positive muon identification with the MUC. “Averages” are obtained by weighting both statistical and systematic uncertainties, but not the third uncertainties, which are dominated by the uncertainty of the D_s lifetime. “LQCD + PDG” represents an expected value, as is explained in the text.

Experiment	Mode	$\mathcal{B}(\%)$	$f_{D_s^+} V_{cs} $ (MeV)
This work	$\tau^+\nu(\pi^+\bar{\nu})$	$5.21 \pm 0.25 \pm 0.17$	$243.0 \pm 5.8 \pm 4.0 \pm 1.0$
This work ($R = 9.75$)	$\tau^+\nu(\pi^+\bar{\nu})$	$5.22 \pm 0.10 \pm 0.14$	$243.2 \pm 2.3 \pm 3.3 \pm 1.0$
BESIII [29]	$\tau^+\nu(\pi^+\bar{\nu})$	$3.28 \pm 1.83 \pm 0.37$	$192.8 \pm 44.2 \pm 10.9 \pm 0.8$
BESIII ($R = 9.75$) [29]	$\tau^+\nu(\pi^+\bar{\nu})$	$4.83 \pm 0.65 \pm 0.26$	$233.9 \pm 15.9 \pm 5.1 \pm 0.9$
CLEO [30]	$\tau^+\nu(e^+\nu\bar{\nu})$	$5.30 \pm 0.47 \pm 0.22$	$245.1 \pm 10.9 \pm 5.1 \pm 1.0$
CLEO [31]	$\tau^+\nu(\pi^+\bar{\nu})$	$6.42 \pm 0.81 \pm 0.18$	$269.7 \pm 17.2 \pm 3.8 \pm 1.1$
CLEO ($R = 9.75$) [31]	$\tau^+\nu(\pi^+\bar{\nu})$	$5.77 \pm 0.36 \pm 0.18$	$255.7 \pm 8.0 \pm 4.0 \pm 1.0$
CLEO [32]	$\tau^+\nu(\rho^+\bar{\nu})$	$5.52 \pm 0.57 \pm 0.21$	$250.1 \pm 13.0 \pm 4.8 \pm 1.0$
BaBar [33]	$\tau^+\nu(e^+(\mu^+)\nu\bar{\nu})$	$4.96 \pm 0.37 \pm 0.57$	$237.1 \pm 8.9 \pm 13.7 \pm 1.0$
Belle [34]	$\tau^+\nu(\pi^+\bar{\nu}, e^+(\mu^+)\nu\bar{\nu})$	$5.70 \pm 0.21^{+0.31}_{-0.30}$	$254.1 \pm 4.7 \pm 7.0 \pm 1.0$
Average ^a	$\tau^+\nu$	5.40 ± 0.19	$247.4 \pm 4.3 \pm 1.0$
This work	$\mu^+\nu$	$0.535 \pm 0.013 \pm 0.016$	$243.1 \pm 3.0 \pm 3.6 \pm 1.0$
BESIII @ 4180 [6]	$\mu^+\nu$	$0.549 \pm 0.016 \pm 0.015$	$246.2 \pm 3.6 \pm 3.4 \pm 1.0$
BESIII [29]	$\mu^+\nu$	$0.517 \pm 0.075 \pm 0.021$	$238.9 \pm 17.5 \pm 4.9 \pm 0.9$
CLEO [31]	$\mu^+\nu$	$0.565 \pm 0.045 \pm 0.017$	$249.8 \pm 10.0 \pm 3.8 \pm 1.0$
BaBar [33]	$\mu^+\nu$	$0.602 \pm 0.038 \pm 0.034$	$257.8 \pm 8.2 \pm 7.3 \pm 1.0$
Belle [34]	$\mu^+\nu$	$0.531 \pm 0.028 \pm 0.020$	$242.2 \pm 6.4 \pm 4.6 \pm 1.0$
Average ^b	$\mu^+\nu$	0.543 ± 0.015	$244.8 \pm 3.5 \pm 1.0$
Average ^c	$\mu^+\nu + \tau^+\nu$...	$246.1 \pm 2.8 \pm 1.0$
LQCD + PDG	243.2 ± 0.5

^aIt excludes “**This work ($R = 9.75$)**”, “BESIII ($R = 9.75$) [29]”, and “CLEO ($R = 9.75$) [31]”.

^bIt excludes “BESIII @ 4180 [6]”.

^cIt excludes “**This work**”, “BESIII @ 4180 [6]”, “BESIII [29]”, and “CLEO [31]”.

- [11] D. J. Lange, *Nucl. Instrum. Methods Phys. Res., Sec. A* **462**, 152 (2001); R. G. Ping, *Chin. Phys. C* **32**, 599 (2008).
- [12] S. Jadach, B. F. L. Ward, and Z. Was, *Phys. Rev. D* **63**, 113009 (2001).
- [13] J. C. Chen, G. S. Huang, X. R. Qi., D. H. Zhang, and Y. S. Zhu, *Phys. Rev. D* **62**, 034003 (2000); Y. Rui-Ling *et al.*, *Chin. Phys. Lett.* **31**, 061301 (2014).
- [14] R. G. Ping, *Chin. Phys. C* **38**, 083001 (2014).
- [15] E. Barberio and Z. Was, *Comput. Phys. Commun.* **79**, 291 (1994).
- [16] R. M. Baltrusaitis *et al.* (MARK III Collaboration), *Phys. Rev. Lett.* **56**, 2140 (1986); J. Adler *et al.* (MARK III Collaboration), *Phys. Rev. Lett.* **60**, 89 (1988).
- [17] M. Ablikim *et al.* (BESIII Collaboration), *Phys. Rev. D* **97**, 072004 (2018).
- [18] M. Ablikim *et al.* (BESIII Collaboration), *Phys. Lett. B*, **744**: 339 (2015).
- [19] Kyle S. Cranmer, *Comput. Phys. Commun.* **136**, 198 (2001). Also available as arXiv:hep-ex/0011057.
- [20] J. P. Alexander *et al.* (CLEO Collaboration), *Phys. Rev. D* **79**, 052001 (2009).
- [21] M. Ablikim *et al.* (BESIII Collaboration), *Phys. Rev. D* **94**, 072004 (2016).
- [22] M. Ablikim *et al.* (BESIII Collaboration), *Phys. Rev. D* **95**, 071102(R) (2017).
- [23] M. Ablikim *et al.* (BESIII Collaboration), *Phys. Rev. D* **99**, 072002 (2019).
- [24] J. C. Yang and M. Z. Yang, *Nucl. Phys.* **B889**, 778 (2014).
- [25] G. Burdman, J. T. Goldman, and D. Wyler, *Phys. Rev. D* **51**, 111 (1995); B. A. Dobrescu and A. S. Kronfeld *Phys. Rev. Lett.* **100**, 241802 (2008).
- [26] J. C. Yang and M. Z. Yang, *Mod. Phys. Lett. A* **31**, 1650012 (2016).
- [27] See Supplemental Material.
- [28] M. Ablikim *et al.* (BESIII Collaboration), *Phys. Rev. D* **81**, 052005 (2010).
- [29] M. Ablikim *et al.* (BESIII Collaboration), *Phys. Rev. D* **94**, 072004 (2016).
- [30] P. U. E. Onyisi *et al.* (CLEO Collaboration), *Phys. Rev. D* **79**, 052002 (2009).
- [31] J. P. Alexander *et al.* (CLEO Collaboration), *Phys. Rev. D* **79**, 052001 (2009).
- [32] P. Naik *et al.* (CLEO Collaboration), *Phys. Rev. D* **80**, 112004 (2009).
- [33] J. P. Lees *et al.* (BABAR Collaboration), *Phys. Rev. D* **82**, 091103(R) (2010); **91**, 019901(E) (2015).
- [34] A. Zupanc *et al.* (Belle Collaboration), *J. High Energy Phys.* **09** (2013) 139.

Supplemental Material

Figures [9-12](#) show our nominal fits to the all six data sets.

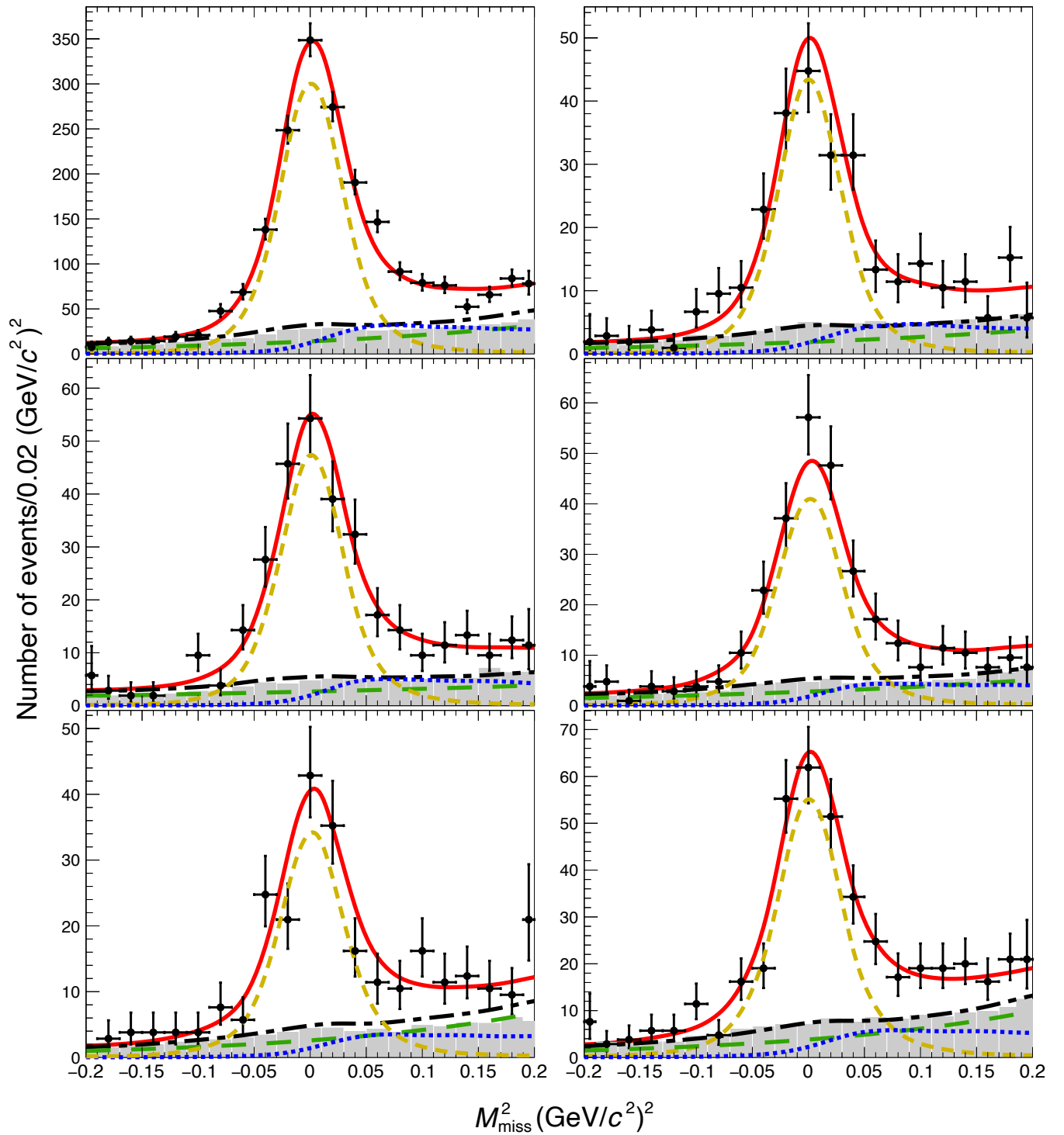


FIG. 9. Projections onto the M_{miss}^2 axis of the two-dimensional fit to 4180 data (top left), 4190 data (top right), 4200 data (middle left), 4210 data (middle right), 4220 data (bottom left), and 4230 data (bottom right) for the μ -like sample. The black points are data, the shaded histograms correspond to the $40\times$ background MC sample scaled to the integrated luminosity of data, and the lines represent the fitted signal and background shapes. The red-solid, orange-dashed, and blue-dotted lines represent the total, $D_s^+ \rightarrow \mu^+ \nu_\mu$, and $D_s^+ \rightarrow \tau^+ \nu_\tau$, while black-dot-dashed and green-long-dashed lines correspond to the total background and the case when both tag and signal sides are misreconstructed, respectively.

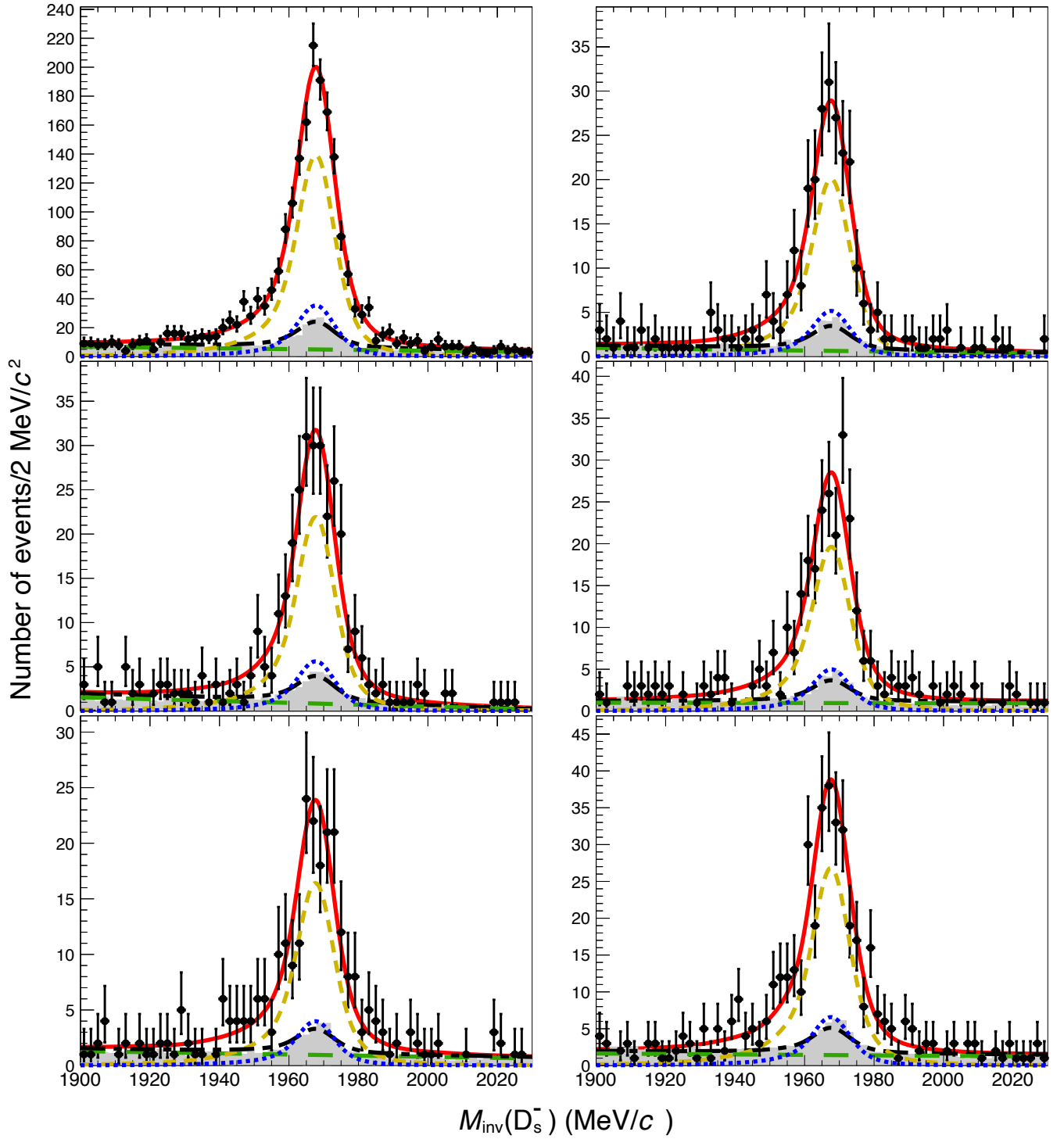


FIG. 10. Projections onto the $M_{\text{inv}}(D_s^-)$ axis of the two-dimensional fit to 4180 data (top left), 4190 data (top right), 4200 data (middle left), 4210 data (middle right), 4220 data (bottom left), and 4230 data (bottom right) for the μ -like sample. The black points are data, the shaded histograms correspond to the $40\times$ background MC sample scaled to the integrated luminosity of data, and the lines represent the fitted signal and background shapes. The red-solid, orange-dashed, and blue-dotted lines represent the total, $D_s^+ \rightarrow \mu^+ \nu_\mu$, and $D_s^+ \rightarrow \tau^+ \nu_\tau$, while black-dot-dashed and green-long-dashed lines correspond to the total background and the case when both tag and signal sides are misreconstructed, respectively.

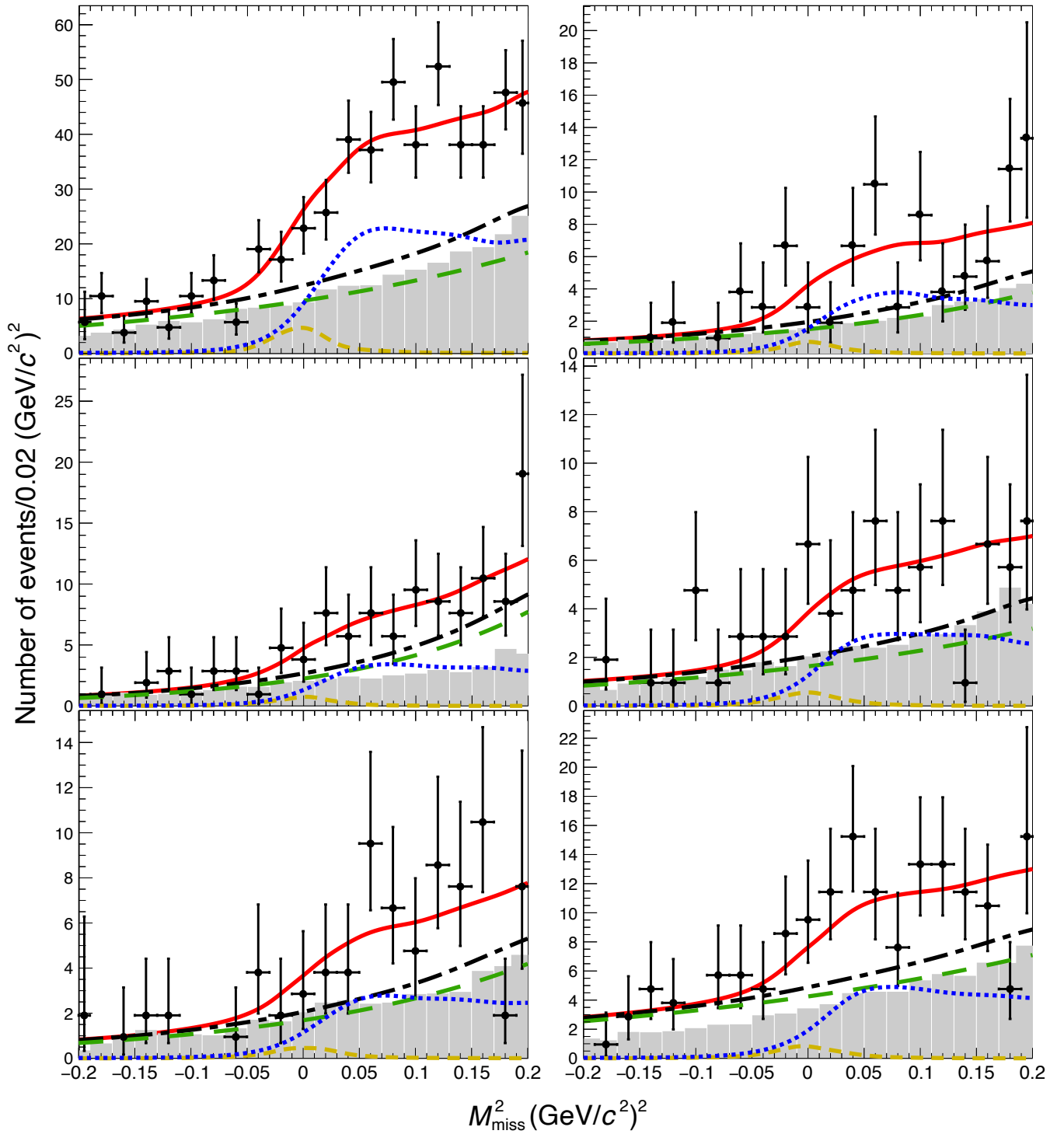


FIG. 11. Projections onto the M_{miss}^2 axis of the two-dimensional fit to 4180 data (top left), 4190 data (top right), 4200 data (middle left), 4210 data (middle right), 4220 data (bottom left), and 4230 data (bottom right) for the π -like sample. The black points are data, the shaded histograms correspond to the $40\times$ background MC sample scaled to the integrated luminosity of data, and the lines represent the fitted signal and background shapes. The red-solid, orange-dashed, and blue-dotted lines represent the total, $D_s^+ \rightarrow \mu^+ \nu_\mu$, and $D_s^+ \rightarrow \tau^+ \nu_\tau$, while black-dot-dashed and green-long-dashed lines correspond to the total background and the case when both tag and signal sides are misreconstructed, respectively.

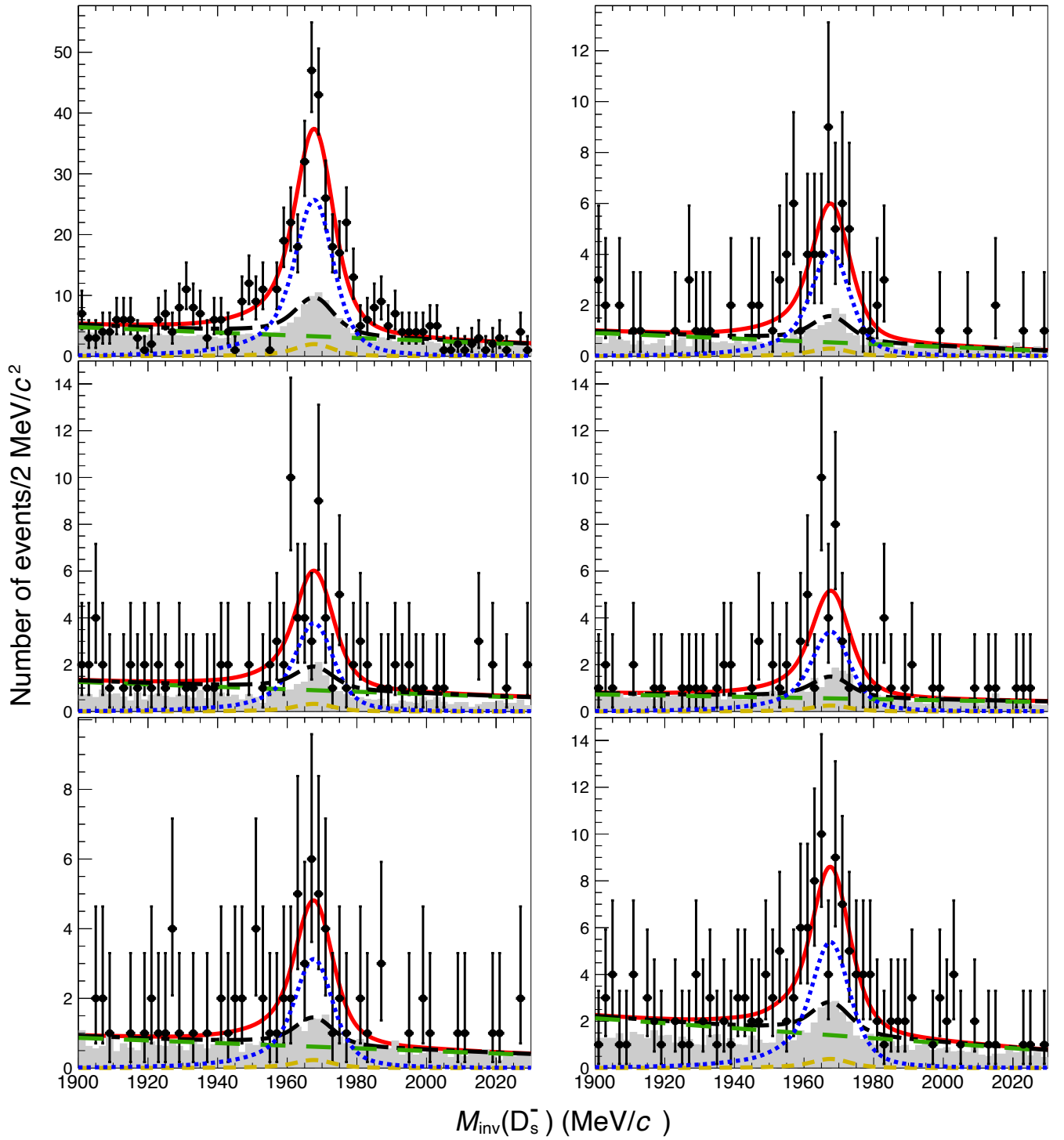


FIG. 12. Projections onto the $M_{\text{inv}}(D_s^-)$ axis of the two-dimensional fit to 4180 data (top left), 4190 data (top right), 4200 data (middle left), 4210 data (middle right), 4220 data (bottom left), and 4230 data (bottom right) for the π -like sample. The black points are data, the shaded histograms correspond to the $40\times$ background MC sample scaled to the integrated luminosity of data, and the lines represent the fitted signal and background shapes. The red-solid, orange-dashed, and blue-dotted lines represent the total, $D_s^+ \rightarrow \mu^+ \nu_\mu$, and $D_s^+ \rightarrow \tau^+ \nu_\tau$, while black-dot-dashed and green-long-dashed lines correspond to the total background and the case when both tag and signal sides are misreconstructed, respectively.